NOISE REDUCTION OF CENTRIFUGAL COMPRESSORS USING ARRAY OF QUARTER WAVELENGTH RESONATORS

A Thesis

by

NAN YE

Submitted to the Office of Graduate and Professional Studies of
Texas A&M University
in partial fulfillment of the requirements for the degree of

MASTER OF SCIENCE

Chair of Committee,	Yong-Joe Kim
Committee Members,	Luis San Andres
	Hamn-Ching Chen
Head of Department,	Andreas A. Polycarpou

August 2014

Major Subject: Mechanical Engineering

ABSTRACT

Noise radiated from high speed centrifugal compressors is becoming a significant design factor. The dominant noise components of a centrifugal compressor can be identified at its blade passing frequencies (BPFs), of which each is a strong tonal noise. Popular noise control methods of a centrifugal compressor includes building of sound insulation enclosure, wrapping of noise insulation materials, mounting of vibration absorbers, and etc. These noise control methods are more effective for broadband noise reduction. Thus, they are generally ineffective to reduce a tonal noise such as the BPF components of the centrifugal compressor. In this thesis, a quarter-wavelength resonator array installed at the outlet pipe of a single-stage centrifugal compressor is studied, which is aimed to reduce the tonal noise of the compressor.

In order to optimally design the quarter-wavelength resonators, numerical simulations are performed by using a commercial software package, COMSOL Multiphysics – Acoustics Module. The optimization procedure is to optimally select geometric design parameters of the quarter-wavelength resonator array such as the diameter and depth of each resonator, and the spacing between the resonators in the axial and circumferential directions. The next procedure is to investigate the effect of four different configurations (i.e., staggered and slanted resonators and the resonators mounted on an expansion pipe and a curved pipe) on the noise reduction performance. Then, the analyses of flow effects on the noise reduction performance of the resonator array are conducted both numerically and experimentally. The high speed air flow induced by the compressor results in wavenumber shifts of noise waves, thus influencing the tonal noise reduction performance of the resonator array. The numerical flow effect analyses are conducted by using commercial software packages, ANSYS FLUENT and ACTRAN. In particular, these software package are used to conduct hybrid aeroacoustic simulations, in which fluid flow and aeroacoustic noise analyses are conducted separately, based on the theory of the Lighthill’s aeroacoustic analogy.

The numerical and experimental results show that the optimally designed quarter-wavelength resonator array can be used to achieve nearly 10 dB noise reduction. From these results, it is also shown that a relation between the Mach number of the airflow and the maximum performance frequency shift is represented as a quadratic curve of $\Delta f = 1918M^2 - 24.21M$ where M is the Mach number and Δf is the frequency shift.

ACKNOWLEDGEMENTS

I would like to express my sincere appreciation to Dr. Yong-Joe Kim for his guidance and patience in advising me to complete my Master of Science degree, for my experience gained while working in the Acoustics and Signal Processing Laboratory as a Graduate Research Assistant, and for the knowledge and understanding leaned in his acoustics course. I would like to thank Dr. Luis San Andres and Dr. Hamn-Ching Chen for their serving on my thesis committee, for the vibration and computational fluid dynamics knowledge gained from their courses, which helped me to conduct my thesis research well. I would also like to thank Huizhi Li and Zheyu Zha for the building of the in-lab experimental test rig and their hard works to conduct the experiments and to process the experimental data. I am also thankful to Dr. Jaeho Choi and Dr. Changwoo Lim at Samsung Techwin for providing the financial support for our research project.

Finally, I would like to sincerely thank my parents for their steadfast support and encouragement. I am exceptionally grateful to my fiancé Petra Yu who has endured time and distance for me.

TABLE OF CONTENTS

LIST OF FIGURES

LIST OF TABLES

CHAPTER I

INTRODUCTION

1.1 OVERVIEW

As the rotational speed of centrifugal compressors increases, it has gained significant interest to reduce noise radiated from the high-speed centrifugal compressors. In particular, it has been known that the Blade Passing Frequencies (BPFs) of compressor's impellers contribute dominantly to the total noise [1]. Most common noise control methods to reduce the noise of a centrifugal compressor include installation of sound insulation enclosure, wrapping of the compressor with noise insulation materials, mounting of vibration absorbers [2], and etc. All of these noise control methods are more effective in reducing broadband noise than tonal noise such as BPF components. As an effective tonal noise control method, the Helmholtz resonators have been widely used to attenuate the tonal noise components [3]. However, they are generally difficulty to be manufactured due to the geometric complexities, bulky to be installed in a compact volume, and ineffective to reduce high frequency components. In this thesis, a tonal BPF noise control method based on the mounting of a quarter-wavelength resonator array at the downstream outlet pipe of a single-stage Samsung Techwin centrifugal compressor is presented to reduce the noise radiated from the compressor effective.

In order to optimally design the quarter-wavelength resonators, the numerical analyses are performed by using a commercial software package, COMSOL Multiphysics – Acoustics Module [4]. This optimal design procedure is used to determine optimal geometric parameters, of the quarter-wavelength resonator array, i.e., the diameter and depth of a single resonator and the spacing between two adjacent resonators in the axial and circumferential directions. The next procedure is to investigate the noise reduction performance of the quarter-wavelength resonator array in various configurations, (e.g., in staggered and slanted distributions and mounted on an expansion pipe and a curved pipe).

Due to the airflow inside of the compressors at a Mach number of 0.1 or higher, the targeted design frequencies of the resonators are shifted [5] due to changes of acoustic impedance [6]. In addition, the noise generated from the turbulent airflow around the resonators, referred to as aeroacoustic noise [7], can negatively affect the acoustic performance of the resonators. Therefore, both the frequency shift and the aeroacoustic noise need to be considered in the design of the resonators. The analyses of the flow effects on noise reduction performance of the resonator array are conducted both numerically and experimentally. The flow effects are analyzed numerically by conducting hybrid aeroacoustic simulations. Two commercial software packages, ANSYS FLUENT and ACTRAN are mainly used for the hybrid aeroacoustic simulations [8,9], based on the theory of the Lighthill's aeroacoustic analogy.

1.2 QUARTER WAVELENGTH RESONATOR

1.2.1 Introduction

The quarter-wavelength resonator array that can be used to reduce the tonal BPF noise components [10] of the centrifugal compressor is usually installed into a duct system as shown in Figure 1.1. In Figure 1.1, each quarter-wavelength resonator is illustrated as a circular cylindrical hole drilled on the inner wall of the duct. It has an open end at the inlet of the resonator and a rigid termination at the other end. An acoustic resonance occurs when the depth of the resonator, *l* is one quarter of the wavelength at the excitation frequency, *f*: i.e.,

$$f = c_0 / 4l \qquad (1.1)$$

where c_0 is the speed of sound.

The incident acoustic wave to the resonator is reflected from the rigid end of the resonator, generating a standing wave, of which the phase is 180 degree out of phase to the incident acoustic wave. This quarter wavelength is thus changing the acoustic impedance to reduce the amplitude of the transmitted wave [10]. In a real resonator, due to the air mass at the open end, the depth of the resonator is slightly shorter than the analytical quarter wavelength as shown in Figure 1.1.

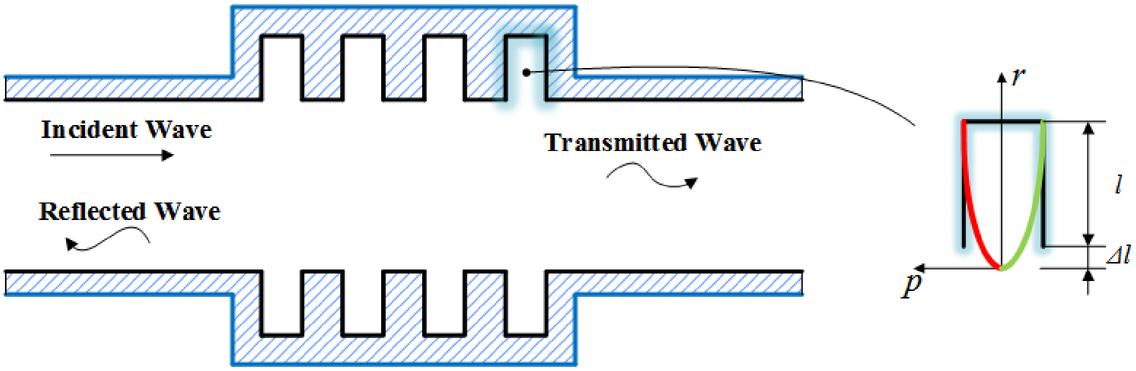

Figure 1.1 Configuration of quarter-wavelength resonator holes flush mounted on inner duct wall.

1.2.2 End Correction Effect

The one end of the resonator where the air blows in and out across the resonator inlet is open to the duct where the acoustic particle velocity is at its maximum. The acoustic pressure at this location becomes the minimum, but not equal to zero due to the air mass closed to the open end. This air mass leads to the length of the cylindrical resonator appears to be acoustically longer than its physical length [11]. This depth increase Δl is referred to as the end correction. In order to compute the resonance frequency of the resonator, the equivalent overall depth (l_{eq}) is equivalent to the sum of the physical depth (l_{hole}) and the additional depth (Δl) due to the end correction.

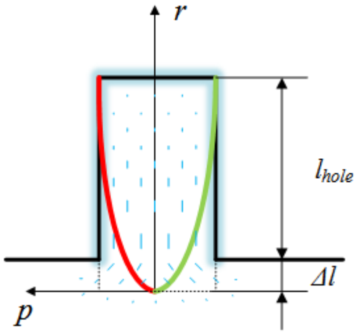

Figure 1.2 End effect of quarter wavelength resonator.

The equivalent acoustic depth (l_{eq}) is then given as

$$\begin{aligned} l_{eq} &= l_{hole} + \Delta l = l_{hole} + 0.6r \\ &= l_{hole} + 0.34\sqrt{A} \end{aligned} \tag{1.2}$$

where r is the equivalent tube radius ($r = (A/\pi)^{0.5}$), A is the cross-sectional area of the open end, and the equivalent overall acoustic depth l_{eq} is one quarter the wavelength of the incident wave ($l_{eq} = \lambda/4$). Hence, the hole depth can be expressed as

$$l_{hole} = \lambda / 4 - 0.34\sqrt{A} \tag{1.3}$$

1.3 COMPUTATIONAL AEROACOUSTICS

1.3.1 Introduction

Computational aeroacoustics (CAA) refers to numerical methods investigating noise generation from either fluid motion or aerodynamic forces [12]. The solution methods to CAA problems are generally categorized into 1) Direct Numerical Simulation (DNS) method [13], 2) Hybrid method [8], and 3) Semi-empirical method [14].

The (DNS) method is the most general approach to solve aeroacoustic problems, analyzing the compressible Navier-Stokes equation directly. In DNS, variables of all scales are solved [13], from the larger acoustic wavelength scales up to the smallest viscous scale. Although this solution method includes noise generation and propagation explicitly and directly, it requires extremely high numerical resolutions due to the large dimensional scale differences between acoustic domain variables and flow domain variables. The computational cost of the DNS method is proportional to Re^3/M^4 (Re is the Reynolds number and M is the Mach number) [13]. Then, the DNS is practically limited to low Reynolds number flows. Combining the requirements of the high resolution and the high computation cost for a high Reynolds number flow, the DNS is unsuitable for any commercial uses.

Regarding to the semi-empirical method, it requires thorough understandings of the problem needed to be solved. Although solutions can be obtained directly in the frequency domain, the accuracy of the solutions from the semi-empirical method are always not satisfactory enough to be applied to real-world applications.

The aeroacoustic analogy, proposed by Sir M.J. Lighthill in the 1950s at the University of Manchester, enables analyses of many aeroacoustic problems. The Lighthill's theory is a foundation of another well-known analogy method proposed by Ffowcs Williams and Hawkings (FWH). The commercial software, ANSYS FLUENT has incorporated a FWH module for CAA computations [15]. This FWH's analogy is based on the assumption that there is no obstacle between sound sources and receivers [15]. Therefore, it is not applicable for solving in-pipe aeroacoustic problems. In the Lighthill's analogy, the interactions from acoustic domain to flow domain is negligible due to a large energy difference [7]. By rearranging the compressible Navier-Stokes equation, Lighthill obtained the aeroacoustic sources tensor [16]. Then, the CAA problems can be solved separately in both the fluid dynamic domain and acoustic domain.

1.3.2 Hybrid CAA Simulations

In Figure 1.3, it is shown the general steps for the hybrid CAA modeling analyses based on the Lighthill's analogy. For the analyses of the mean airflow effects, which account for the frequency shift, the flow domain solution data are first obtained from CFD simulations conducted by using ANSYS FLUENT and then they are imported into acoustic meshes built in ACTRAN. For the analyses of the turbulent noise, the aeroacoustic noise source information will be extracted from unsteady CFD simulation data. Such a hybrid analysis method is theoretically based on the Lighthill's aeroacoustic analogy [8 16] which is introduced in Chapter III.

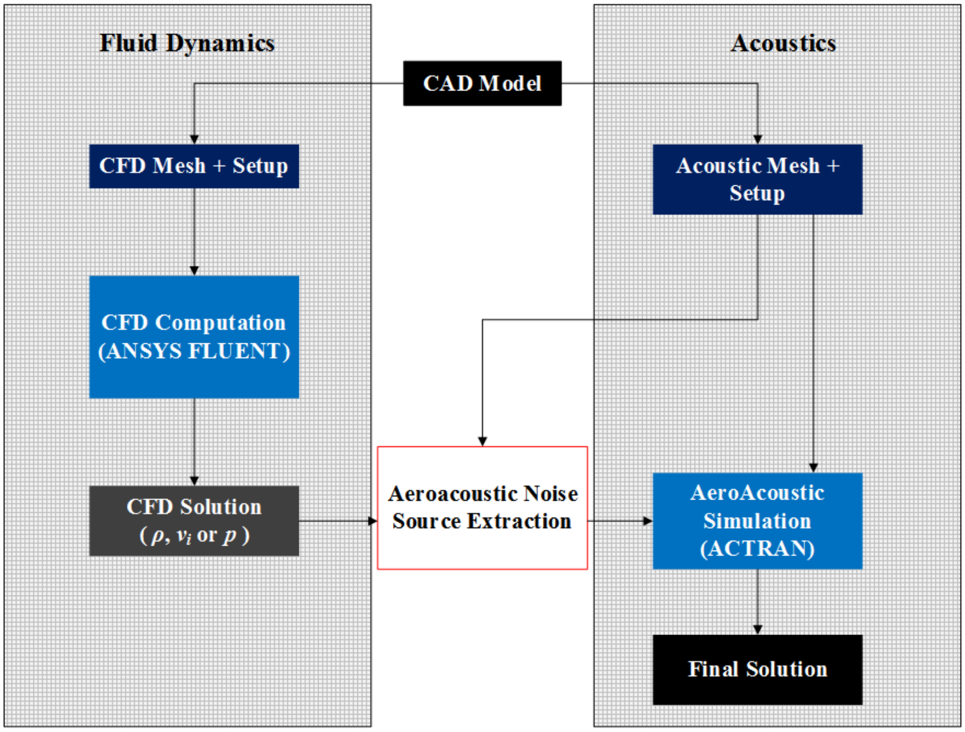

Figure 1.3 ACTRAN process for the computation of aeroacoustic sources from unsteady CFD results.

1.3.3 Aeroacoustic Noise Extraction

The total pressure obtained from a CFD simulation after applying a turbulence model, e.g., k-ε, k-ω, LES and etc., can be separated into two parts, the static flow pressure, p_0 and the acoustic fluctuation pressure p', i.e.,

$$p = p_0 + p' \tag{1.4}$$

where p_0 is assumed to be weakly depending on time and p' is extremely small. In general, the magnitude ratio of the acoustic pressure to the static pressure is much smaller than numerical computation errors. Thus, the acoustic pressure extracted directly from the CFD-predicted pressure data is erroneous. For example, assume the acoustic pressure of 90 dB in a compressed air with a static pressure of 5 bars (approximately, 500 kPa). Then, the magnitude ratio is 1.2×10^{-6}. This means that the CFD simulation should have less than a computational error of 1.2×10^{-4} % in predicting the total pressure, which is extremely challenging even with modern computational resources.

The most commonly used way for aeroacoustic noise source extractions is the hybrid simulation method based on the Lighthill's aeroacoustic analogy, the governing equation describing the analogy concept is shown as below:

$$\frac{\partial \rho v_i}{\partial t} + a_0^2 \frac{\partial \rho}{\partial x_i} = -\frac{\partial T_{ij}}{\partial x_j} \tag{1.5}$$

where T_{ij} is the Lighthill's stress tensor. Since the Lighthill's stress tensor, T_{ij} can be represented in terms of fluid flow velocities, this hybrid approach is not relying on the small acoustic variables. Thus, it can be used to obtain relative accurate acoustic information from CFD solutions that include even small numerical errors. This hybrid simulation method is mainly taken into application in this research.

CHAPTER II

OPTIMAL DESIGN OF RESONATOR ARRAY

2.1 OPTIMAL DESIGN

2.1.1 General Procedure

The geometric shape of a quarter-wavelength resonator array decides the frequency of the tonal noise reduction. Thus, an optimal design of resonators' geometric parameters is required to maximize the noise reduction performance. As shown in Figure 2.1, the geometric design parameters of a single quarter-wavelength resonator include the diameter (d) and the depth (l). The design parameters of the resonator array include the axial spacing (ΔL), the circumferential angular spacing ($\Delta\theta$), and the number of axial layers (N). Here, it is proposed to determine these design parameters by conducting the numerical analyses described below.

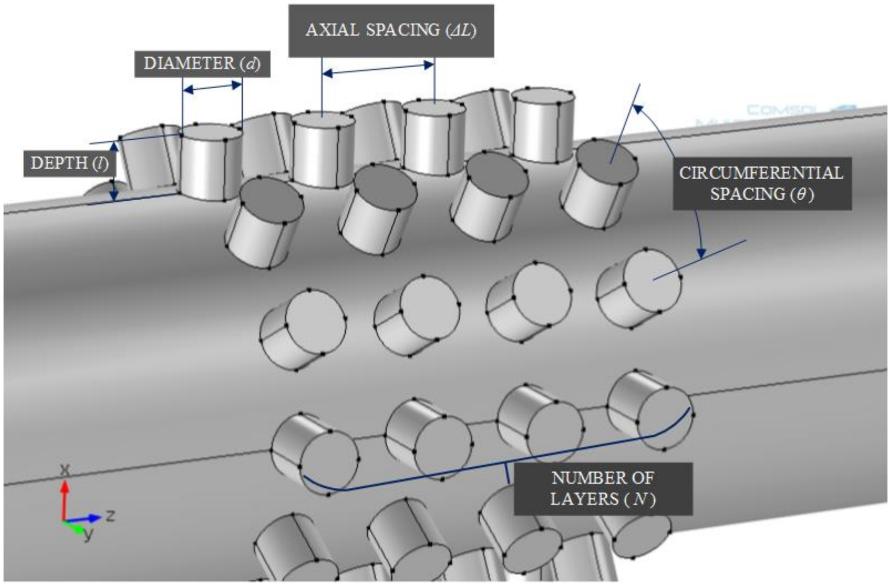

Figure 2.1 Design parameters of quarter wavelength resonators.

In order to obtain the optimal design parameters, a 3-D finite element model is built in a commercial software package, COMSOL Multiphysics - Acoustics Module. Although this software package cannot be used to analyze aeroacoustic fields generated by the airflow inside the duct, the static acoustic fields inside the pipe with the quarter-wavelength resonators can be simulated computationally efficiently when compared to other software packages. This computational efficiency is critical when the geometric parameters need to be varied frequently for the identification of the optimal design.

In order to build the COMSOL model, a CAD model, such as in Figure 2.1, is imported into COMSOL Multiphysics. Then, the entire domain is set as air of which the static pressure and density are corresponding to a specific operation condition to be analyzed. At the inlet boundary shown in Figure 2.2, a plane wave excitation is applied at the fundamental BPF. The excitation pressure amplitude is set to 1 Pa for the convenient calculation of incident sound intensity (i.e., $I_{zai} = 1/2\rho c_0$). A plane wave radiation boundary, that is equivalent to the non-reflecting boundary condition, is set at the outlet boundary (see Figure 2.2). However, regarding to flow effect analyses discussed in Chapter III, random incident waves having higher acoustic modes in both the circumferential and radial directions are used for the analysis of the airflow effects. The random incident excitation represent real excitation cases in a way much closer than the plane wave excitation, even though it requires higher computational cost. The plane wave excitation is functional enough for the present optimal design procedure. The performance of the optimal design obtained by using the plane wave excitation will then be validated for the case of the random incident excitation.

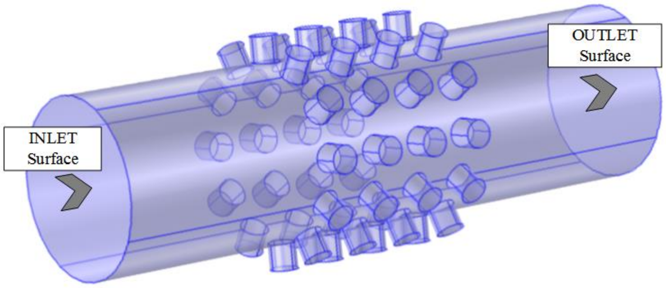

Figure 2.2 Inlet and outlet surfaces of simulation model.

As for the post-processing of the resulting numerical data, sound transmission loss (TL) is calculated to represent the noise performance of the resonators that is defined as the ratio of the spatially-averaged, incident to transmitted sound intensities expressed as,

$$TL = 10\log 10(I_{inc} / I_{trans}) \tag{2.1}$$

For the spatially-averaged incident sound intensity in the upstream of the resonator array, it is already calculated as $1/2\rho c_0$, which only depends on the air density and speed of sound in the air, for the plane wave excitation. For the calculation of the spatially-averaged sound intensity in the downstream pipe, three axial cross-sectional planes are selected at the downstream area. The summation of the sound intensities on all nodes on each cross-sectional plane is calculated first and it is then divided by the total areas to calculate the spatially-averaged sound intensity (I_{zat}). Then, the three intensities on the three planes are averaged again to obtain the spatially-averaged, transmitted sound intensity.

Since the aforementioned numerical model will be built for a single set of the geometric design parameters, a method for analyzing the model with different sets of geometric design parameters is needed to obtain the optimal design parameters. In this case, the “Parameter Sweep” function built in COMSOL Multiphysics is employed along with the automatic control of the “LiveLink for Matlab” module [17]. During this process, the numerical model is first analyzed in COMSOL. Then, the solution data are exported into Matlab for calculating the TL and storing the TL results. For the next geometric case, the cached data in COMSOL is cleaned and the model with different geometric design parameters is loaded by using the Parameter Sweep. This process is iterated automatically until all the geometric cases are analyzed to obtain the optimal design parameters.

2.1.2 Periodic Condition and Mesh Sizes

In order to reduce the computational cost, one part of the model as shown in Figure 2.3 is taken into simulation instead of the entire 3D model. Before simulation, a periodic condition is added at the axial cut plane surface. Since the geometry is axisymmetric, it is possible to perform simulation with respect to only partial CAD model. In this way, the computational cost and time is reduced largely due to the large amount of reduction of degree of freedoms (DOF).

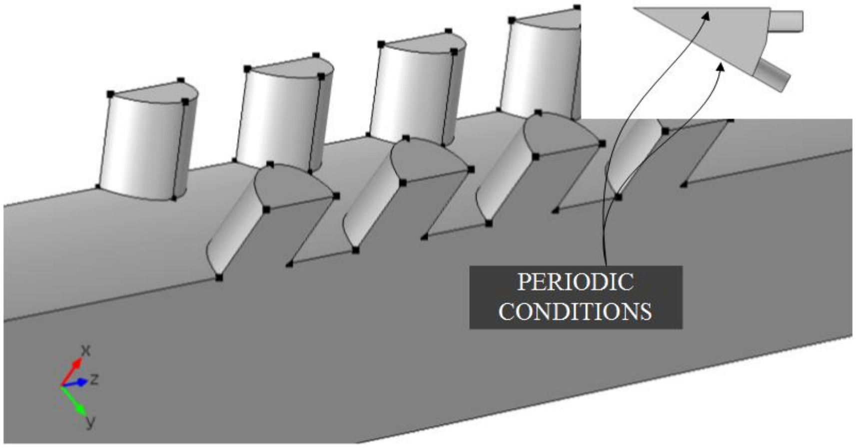

Figure 2.3 Geometric model with periodic conditions.

Regarding to mesh generation, the maximum mesh size is set as 1/8 of the wavelength, which means that there are at least 8 nodes per wavelength in finite element computations. In Figure 2.4, it is shown the unstructured meshing of resonator model. The linear tetrahedral element is used in meshing. Inside the resonators and around the places with sharp geometry changes, there are more elements and the mesh size is much smaller. Since the geometry parameters (e.g., depth, diameter, axial spacing and etc.) are dominant factors deciding the noise reduction performance of the mechanism, it is of much importance to guarantee that the resonator shape is accurately modeled by the meshes.

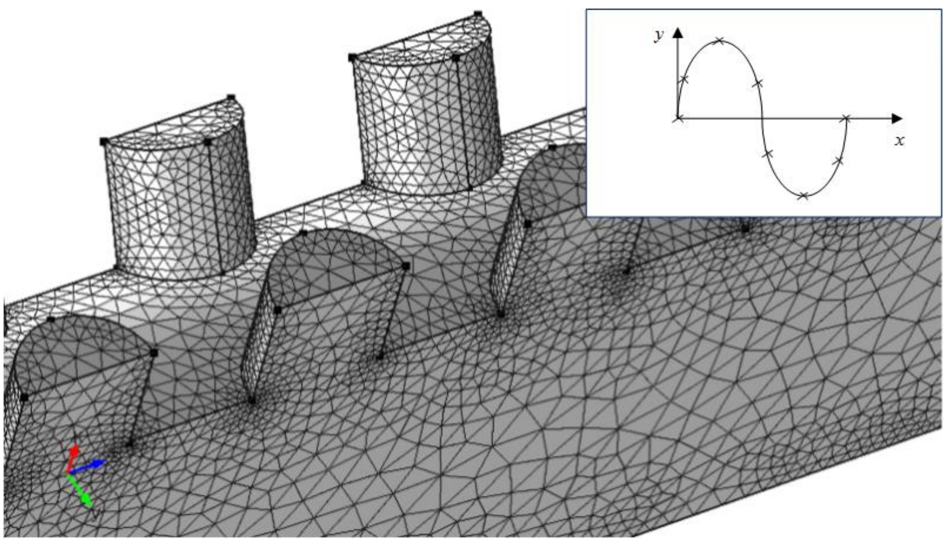

Figure 2.4 Meshing of geometry model in optimal design.

2.2 OPTIMIZATION RESULTS

2.2.1 Resonator Depth and Diameter

The first step of optimization procedure involves obtaining the optimal combination of the resonator's depth and diameter. From the aforementioned analytical solution, it is know that the depth of the resonators should be close to the effective quarter wavelength when considering the end correction effect discussed in Chap. 1.2.2.

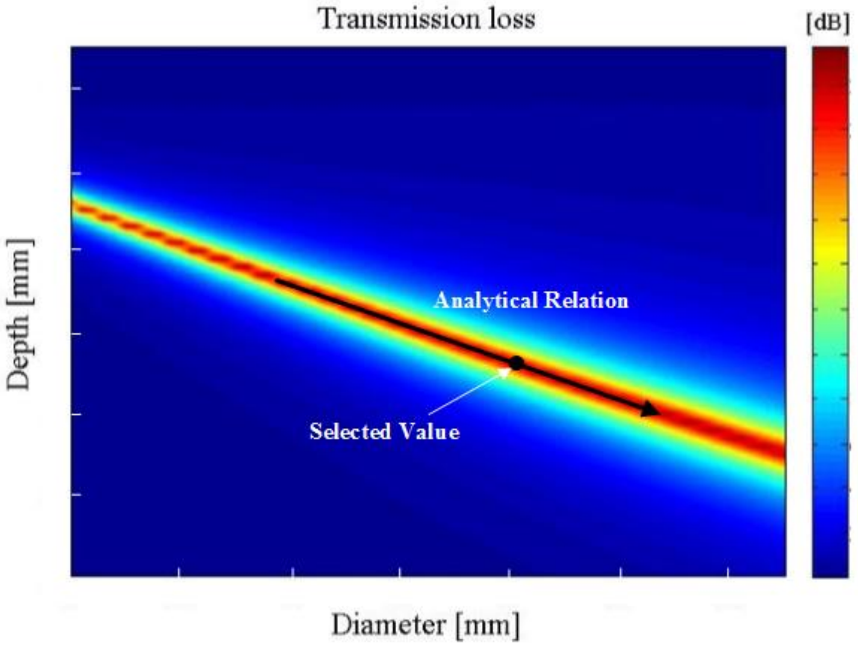

Figure 2.5 Transmission loss with respect to variation of depths and diameters of resonators, and selected data point on analytical effective quarter wavelength.*

Figure 2.5 shows the predicted transmission loss (TL) values as a function of the resonator's depth and diameter. In order to generate this plot, the model with single layer of resonators is used, with circumferential spacing of 30 degree. Throughout the numerical simulation procedure, the operation conditions are set as sound speed c_0 equals 340 m/s, air density ρ = 1.225 kg/m3 and ambient pressure P = 1atm, which are same as the environment for the experiment.

It can be seen that the analytical solution with the effective quarter wavelength curve (shown as the black line with the arrow in Figure 2.5 is on the red area where the TL value are maximized. Therefore, it also can be concluded that the numerical method

---

* All dimensional parameters for recreation of designed model are removed due to confidentiality agreement of research sponsor, Samsung Techwin Co. Detailed geometric information are shown in Appendix B, which are deleted in the final publishable version.

is validated against the analytical solution, indicating the optimal length and diameter can be identified by using both the analytical and numerical methods.

Here, the optimal resonator depth and diameter are chosen as the value at the black point in Figure 2.5. The criteria of this selection is to obtain a TL value up to 22 dB, and at the same time, the diameter of resonators is not too large, so that it is guaranteed that the airflow inside of a pipe will not be affected after installation of resonators. The selection is also based on the shape of the red area in Figure 2.5 where the range of the optimal depth is getting narrower with a smaller diameter. Thus, the diameter should not be too small to avoid the acoustic performance degradation induced by any small machining errors in the hole dimensions.

2.2.2 Circumferential Spacing

After the selection of the optimal resonator depth and diameter, the circumferential spacing ($\Delta\theta$) shown in Figure 2.6 is optimally determined by varying the circumferential spacing in the COMSOL model with a single layer of the holes ($N = 1$). In this procedure, the depth and diameter is fixed at the optimal values obtained from the previous procedure. The discrete angles at 18^0, 22.5^0, 36^0 … etc. in the following optimization result of Figure 2.6 are to guarantee that the holes are distributed evenly along the circumference of the inner pipe surface. Then the TL value is evaluated at each circumferential angle.

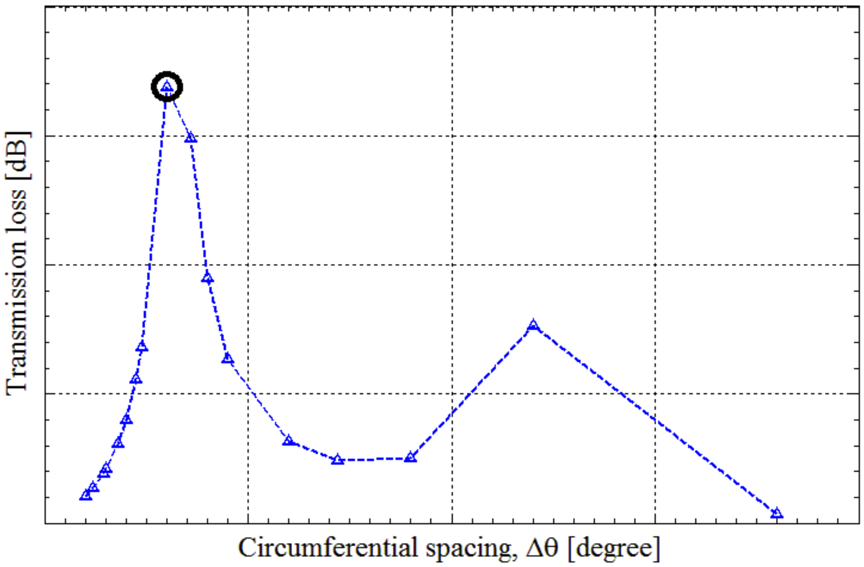

Figure 2.6 Transmission loss with respect to circumferential spacing.

2.2.3 Axial Spacing and Number of Layers

Under the three numbers of layers (*N*) (e.g., 4 layers, 5 layers and 6 layers), the optimal axial spacing (ΔL) is obtained where the resulting TL is maximized. The TL performance is investigated with respect to the axial spacing ranges from 20 mm to 50 mm as shown in Figure 2.7.

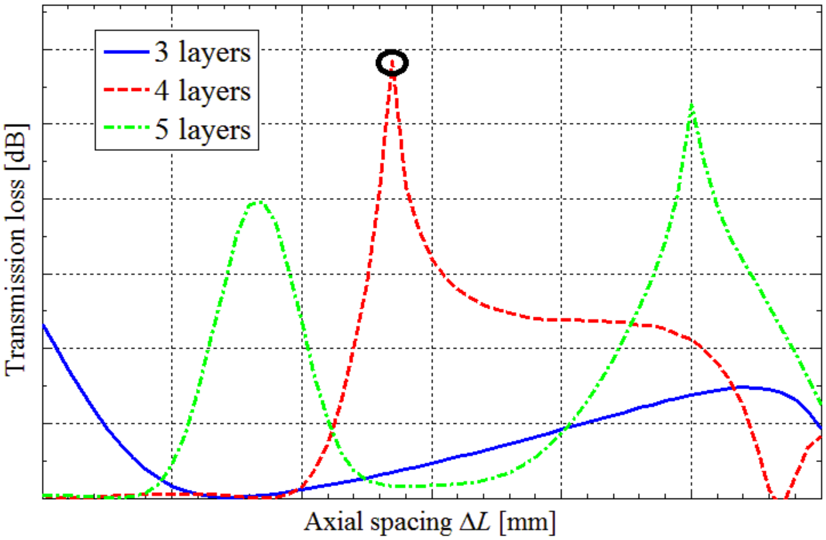

Figure 2.7 Transmission loss with respect to axial spacing at various number of layers.

2.2.4 Frequency Response

After optimizations, all the parameters related to the configurations of the quarter wavelength resonators are determined. Applying all these geometric parameters on the model for simulation, the frequency response of transmission loss result is obtained. As shown in Figure 2.8, there is one maximum resonance peak at the frequency of 3600 Hz, which is the target frequency before the design of resonators. From numerical results, it is predicted that TL of 31 dB can be obtained by using the optimal design of the resonators. But the result is needed to be validated by experiment further.

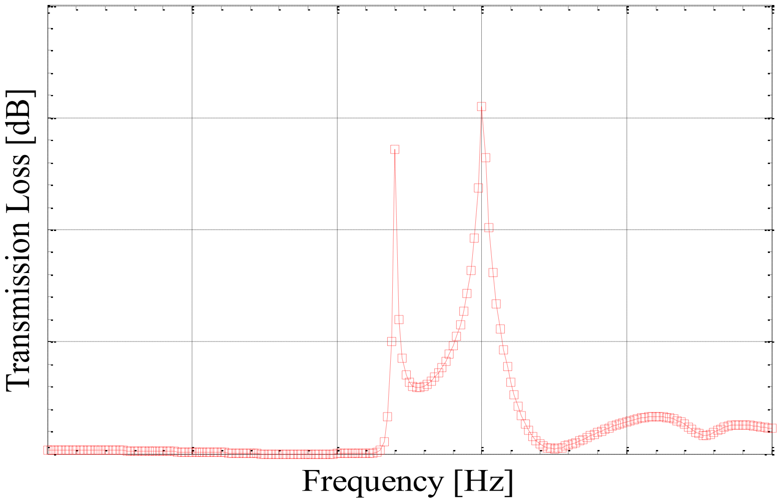

Figure 2.8 Frequency response of transmission loss of resonators after optimal design.

2.3 SENSITIVITY ANALYSIS

This TL sensitivity analysis procedure is to investigate how much noise reduction performance is changed when the design parameters are slightly varied from their optimal values. Here, the maximum deviation of the diameter and depth from their optimal values is set to ± 5%. The sensitivity analysis results are shown in Table 2.1.

Table 2.1 TL [dB] with variations of resonator depth and diameter.

Dim. Error	- 5.00 %	- 2.50 %	- 1.25 %	Optimal Diameter	+ 1.25 %	+ 2.50 %	+ 5.00 %
- 5.00 %	2.453	3.709	5.725	9.489	17.24	19.45	10.56
- 2.50 %	2.892	4.409	6.986	11.68	22.70	15.22	8.810
-1.25 %	3.400	5.255	8.427	14.48	23.20	12.19	7.438
- 1.00 %	4.022	6.280	10.28	18.87	18.27	10.11	6.313
- 0.25 %	4.756	7.534	12.65	24.00	14.21	8.509	5.400
Optimal Depth	5.180	8.269	14.09	24.05	12.91	7.937	4.979

Table 2.1 Continued

Dim. Error	- 5.00 %	- 2.50 %	- 1.25 %	Optimal Diameter	+ 1.25 %	+ 2.50 %	+ 5.00 %
+ 0.25 %	5.644	9.062	15.83	21.71	11.67	7.316	4.604
+ 1.00 %	6.612	10.98	20.41	17.014	9.778	6.176	3.977
+ 1.25 %	7.905	13.44	24.32	13.64	8.289	5.286	3.386
+ 2.50 %	9.561	16.51	20.44	11.27	7.060	4.551	2.872
+ 5.00 %	11.41	20.83	16.63	9.603	6.131	3.951	2.466

For a better presentation of the TL sensitivity results, the TL sensitivity results in Table 2.1 are normalized with that of the optimal point, resulting in the TL value to be zero at the optimal point. The normalized TL results are shown in Table 2.2 and Figure 2.9. In Figure 2.9, it is shown that the normalized TL value variations in the vertical direction (i.e., the resonator diameter) are smaller than those in the horizontal direction (i.e., the resonator's depth). Therefore, it can be concluded that the noise reduction performance is less sensitive to the variation of the diameter (*d*) than the depth (*l*) when the same percentage variation is present in both the design parameters, indicating that the resonator hole depth should be more precisely machined than the diameter.

Table 2.2 Normalized TL [dB] with variations of resonator depth and diameter.

Dim. error	- 5.00 %	- 2.50 %	- 1.25 %	Optimal diameter	+ 1.25 %	+ 2.50 %	+ 5.00 %
- 5.00 %	21.60	20.34	18.32	14.56	6.810	4.596	13.49
- 2.50 %	21.16	19.64	17.06	12.37	1.345	8.825	15.24
-1.25 %	20.65	18.79	15.62	9.565	0.845	11.86	16.61
- 1.00 %	20.03	17.77	13.77	5.178	5.782	13.94	17.74
- 0.25 %	19.29	16.52	11.40	0.048	9.841	15.54	18.65
Optimal depth	18.87	15.78	9.959	0.000	11.14	16.11	19.07
+ 0.25 %	18.41	14.99	8.213	2.344	12.38	16.73	19.45

Table 2.2 Continued

Dim. error	- 5.00 %	- 2.50 %	- 1.25 %	Optimal diameter	+ 1.25 %	+ 2.50 %	+ 5.00 %
+ 1.00 %	17.44	13.07	3.637	7.041	14.27	17.87	20.07
+ 1.25 %	16.14	10.61	-0.273	10.41	15.76	18.76	20.66
+ 2.50 %	14.49	7.540	3.606	12.78	16.99	19.50	21.18
+ 5.00 %	12.64	3.217	7.422	14.44	17.92	20.10	21.58

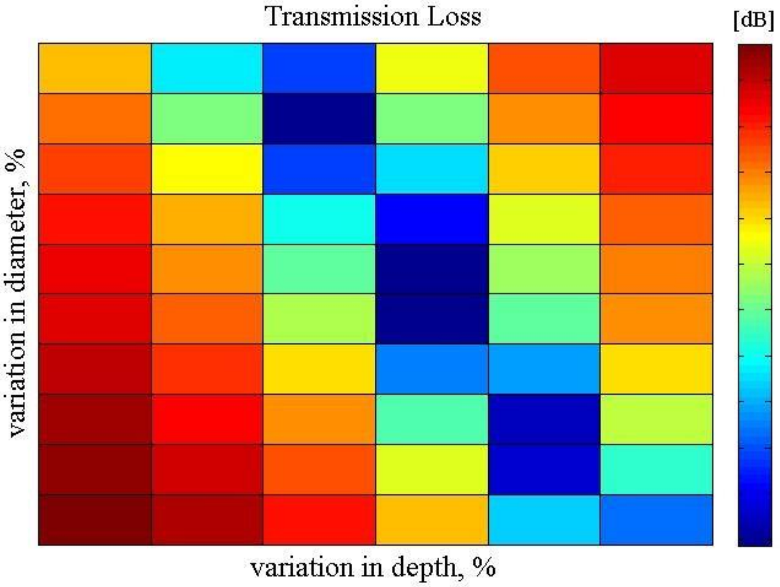

Figure 2.9 Normalized TL with variations of resonator depth and diameter.

In order to better understand the effects of the design parameter variations on the TL performance, Figure 2.10 shows the resonance frequency shifts when the resonator depth and diameter are varied. The black dashed lines in these figures represent the design target frequency of 3600 Hz. From the center plot, it can be seen that at the optimal design parameters, the maximum noise reduction location of the resonators is in coincidence with the target frequency. When the geometry parameters are varied from their optimal values, the maximum performance peak shifts either to the left or to the right, resulting in the lower noise reduction performance at the design target frequency.

In the TL plots in Figure 2.10, in addition to the peaks around the target frequency of 3600 Hz, there is another peaks at the lower frequencies around 3470 Hz. These peaks are not present with a single layer of the resonators. Thus, these additional peaks are generated by the multiple layers of the resonators: i.e., the total axial length of the resonator array is in control of the additional peak location. This effect can be taken advantage of in the near future when some additional frequency components need to be reduced in addition to the noise components at the main target frequency.

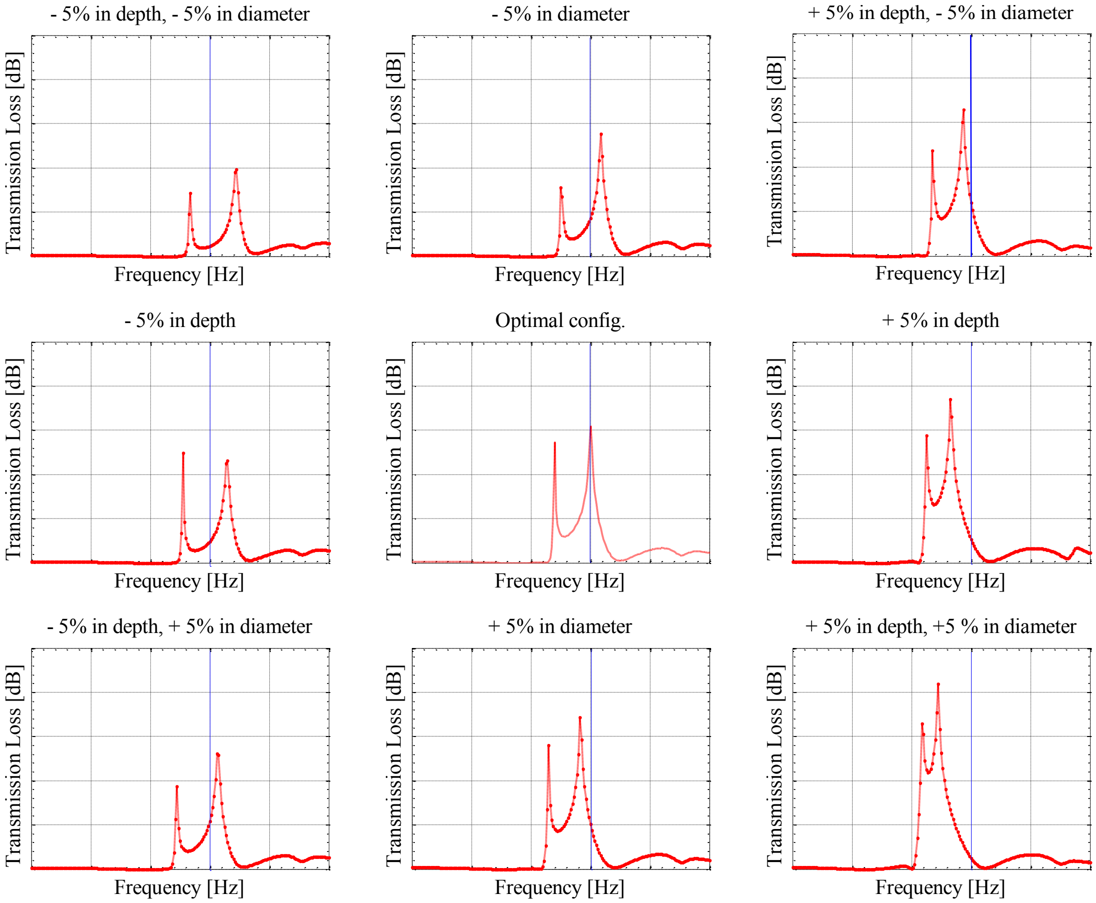

Figure 2.10 Shift of TL peaks with variations of resonator diameter and depth.

2.4 EFFECTS OF RESONATOR DISTRIBUTIONS

2.4.1 Staggered Distribution

The performance of the staggered resonators shown in Figure 2.11 is investigated. The twisted angle (α) between two adjacent layers of the resonators is set to 15°. In this procedure, the entire 3-D model is used in numerical simulation instead of the partial model with periodic conditions, since there is no long symmetric characteristics with twisted resonator array.

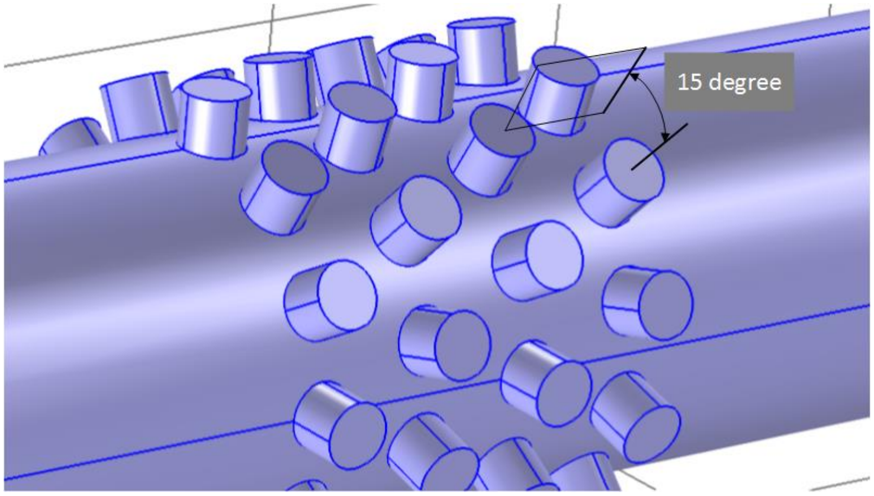

Figure 2.11 Staggered distribution of resonators with twisted angle of 15 degree.

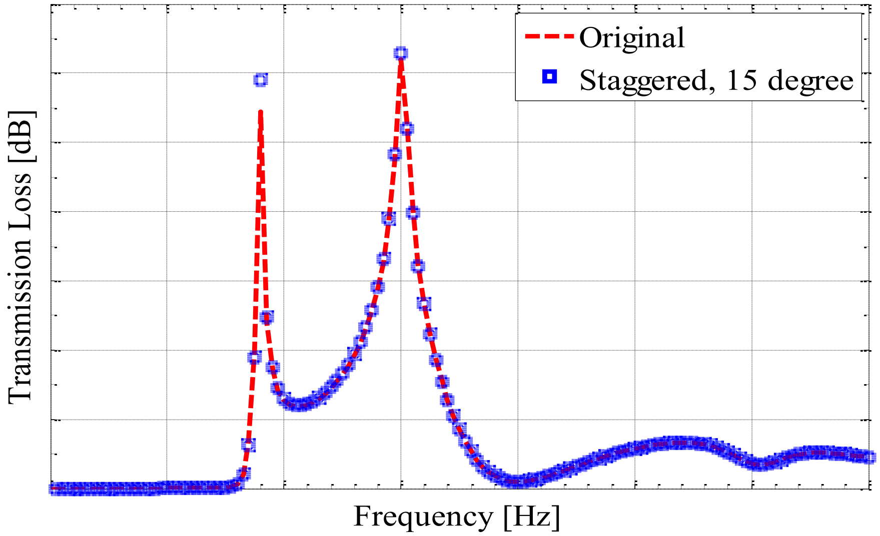

Figure 2.12 Simulated TL results of staggered resonators.

From the simulation results shown in Figure 2.12, it can be seen that there is no appreciable difference between the performance of the staggered and original resonator distributions. Considering the manufacturing of the staggered distribution of resonators is harder than the original distribution, the cost and efficiency issues, the staggered distribution of resonators is not recommended.

2.4.2 Slanted Resonators

Slanted resonators disturb the airflow inside the pipe less than the upright resonators. Here, the performance of the slanted resonators with a slanted angle of $\beta = 45°$ is investigated as shown in Figure 2.13.

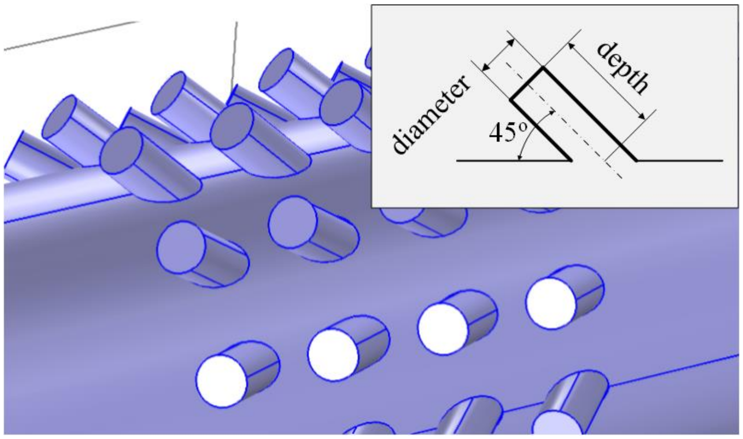

Figure 2.13 Slanted resonator array with angle of 45 degree.

In order to obtain the optimal design of slanted resonators, an optimization procedure similar as that for the original distribution of resonators is performed.

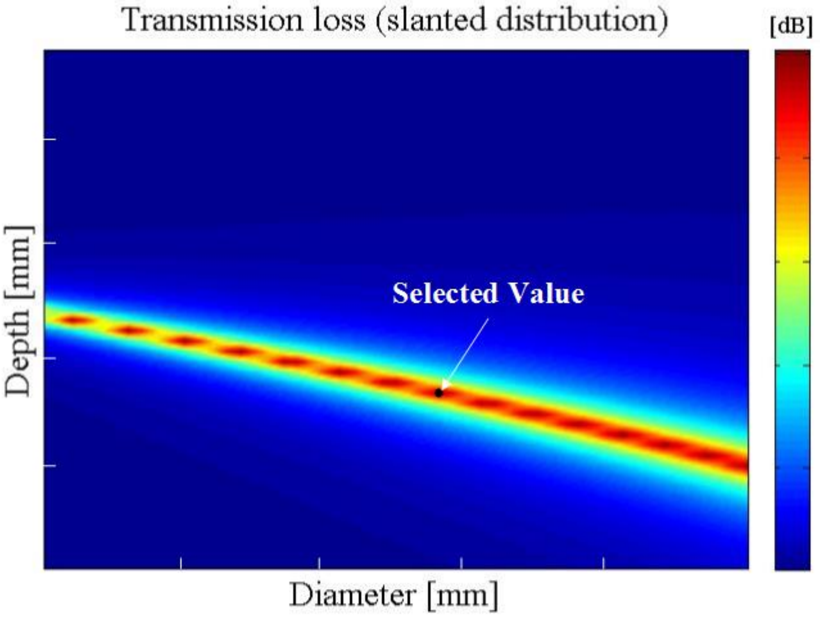

Figure 2.14 TLs versus resonator depth and diameter, slanted distribution.

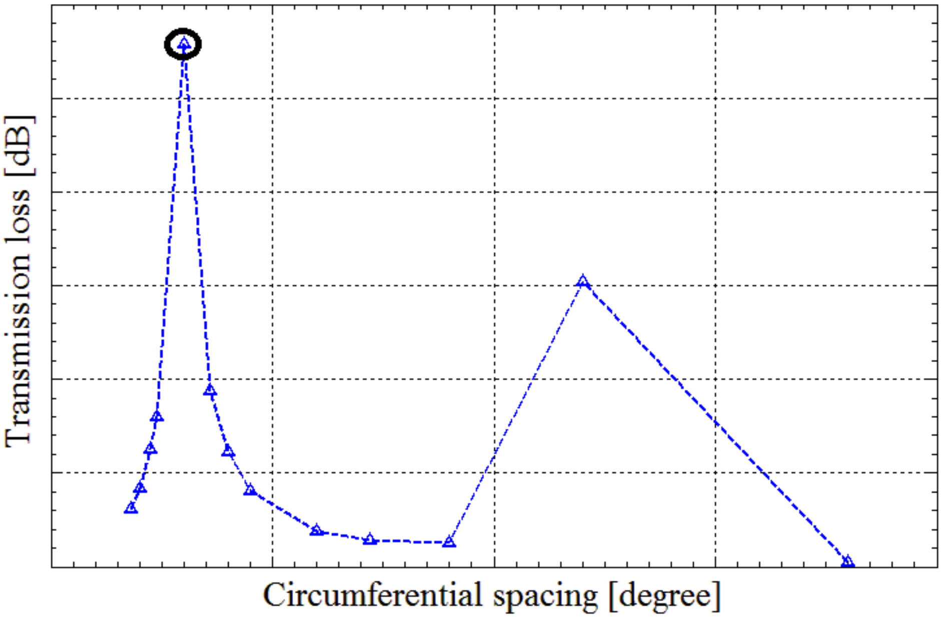

Figure 2.15 TL versus circumferential spacing of slanted resonators.

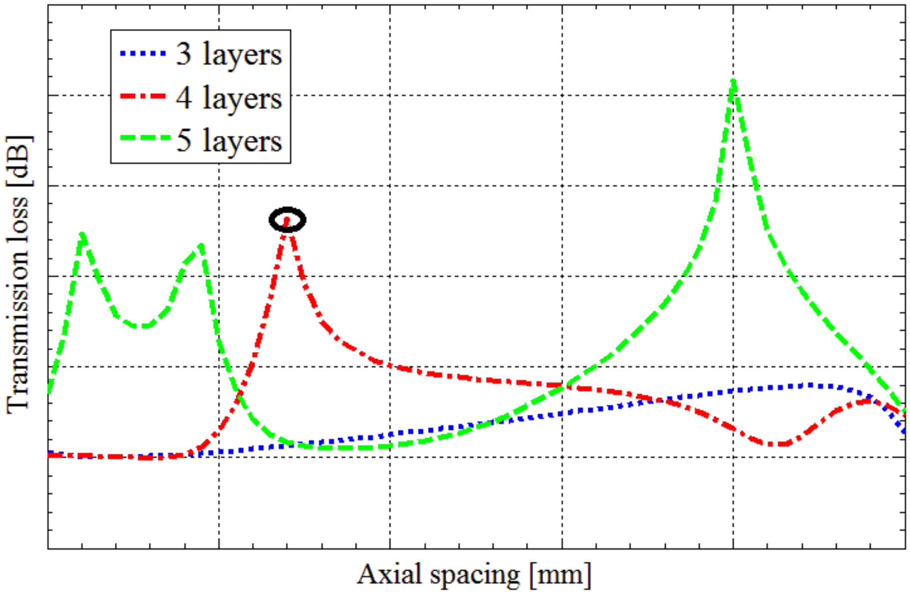

Figure 2.16 TL versus axial spacing of slanted resonators at various number of layers.

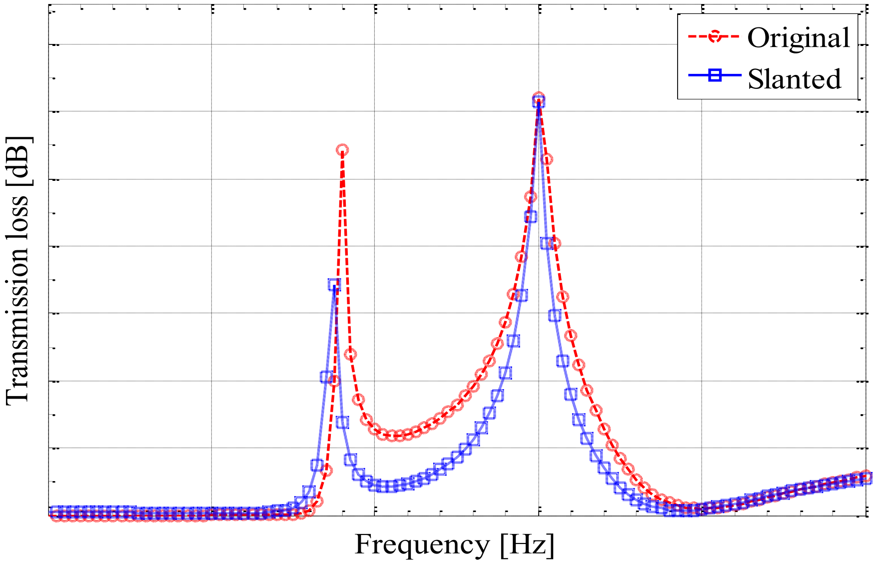

Figure 2.17 TLs of original upright and slanted resonators.

In Figure 2.14 to Figure 2.16, the optimization results of the slanted resonators are shown. From these optimization results, the optimal design parameter are determined.

Then, the performance of the optimally designed, slanted resonators are compared with that of the original upright resonators. Figure 2.17 shows the TL performance comparison between the slanted resonators and the original straight resonators. From this figure, it can be seen that the slanted resonators performs equivalently to the original resonators at the main target frequency of 3600 Hz, although the additional performance peak of the slanted resonators around 3570 Hz is approximately 10 dB smaller than that of the original resonators. It should be also noted that the performance frequency bands of the slanted resonators are smaller than those of the original ones. Thus, the slanted resonators may be preferred in terms of aerodynamic performance. However, fine frequency tuning is required for the slanted resonators to achieve equivalent acoustic performance to the original upright resonators.

2.4.3 Pipe Curvature Effects

For the resonators installed on a curved pipe as shown in Figure 2.18, the noise reduction performance of the resonators is investigated in this section. Here, the curvature of the curved pipe is set to 2 m. The simulation results of the resonators install in the curved pipe are compared with those in the straight pipe as shown in Figure 2.19. From this figure, it can be seen that the TL performance of the curved pipe case is reduced when compared with the straight pipe case. Thus, it is recommended that the designed resonators are installed in a straight pipe section in order to maximize their noise reduction performance.

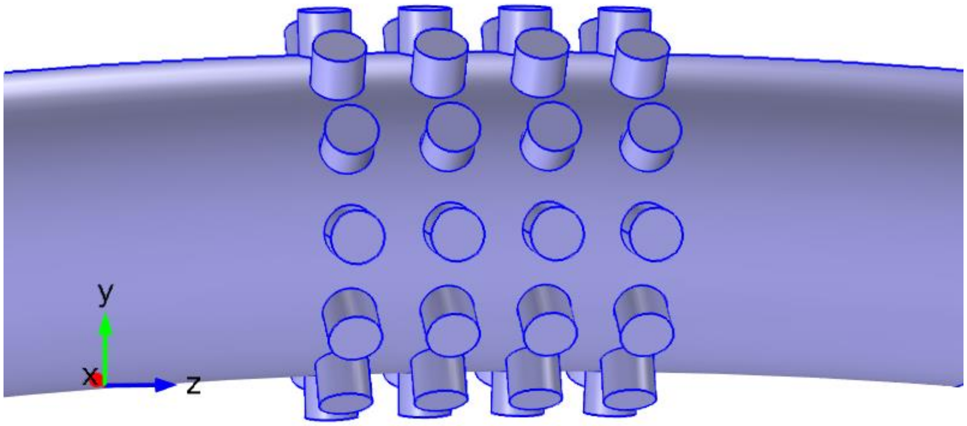

Figure 2.18 Model of resonators in pipe with curvature of 2 m.

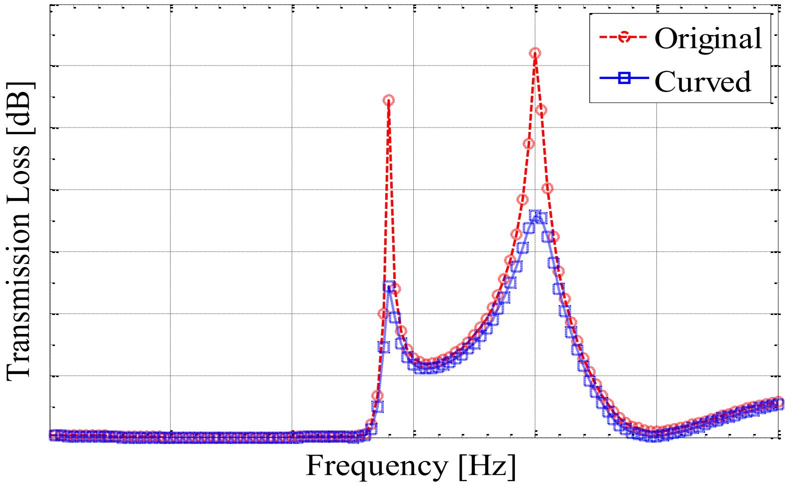

Figure 2.19 TLs of original pipe and curved pipe.

2.4.4 Effects of Pipe Expansion

In addition to the above configurations of the resonators, the effect of an expanded pipe model is investigated. The shape of the expanded pipe model is shown in Figure 2.20. The expansion slope of the pipe wall is set to 5°.

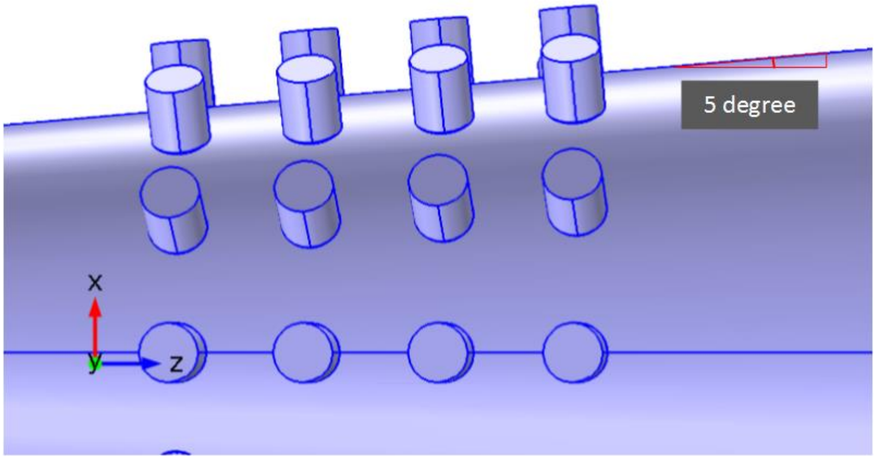

Figure 2.20 Sketch of expanded pipe model.

Similar to the previous optimization procedure, an optimization procedure is also applied to obtain the optimal design parameters of the resonators in the expanded pipe. In Figure 2.21, the optimization results for the determination of the design parameters are shown. Figure 2.22 shows the TL results of the expansion case after the optimization on top of the original TL results with the straight pipe. As shown in Figure 2.22, the maximum TL of the expanded pipe case is approximately 24 dB and the TL band around the maximum performance frequency is much wider than that of the straight pipe case, which indicates that the noise reduction performance is less sensitive to the design parameter variation than the original straight pipe configuration. Once the performance of the optimally designed resonators installed on the expanded pipe is experimentally validated, these resonators can be used to reduce higher noise levels than ones in the straight pipe. Physically, the expansion results in gradual acoustic impedance mismatching, increasing the magnitude of reflected noise waves. Then, the magnitude of transmitted waves can be reduced to improve the noise reduction performance.

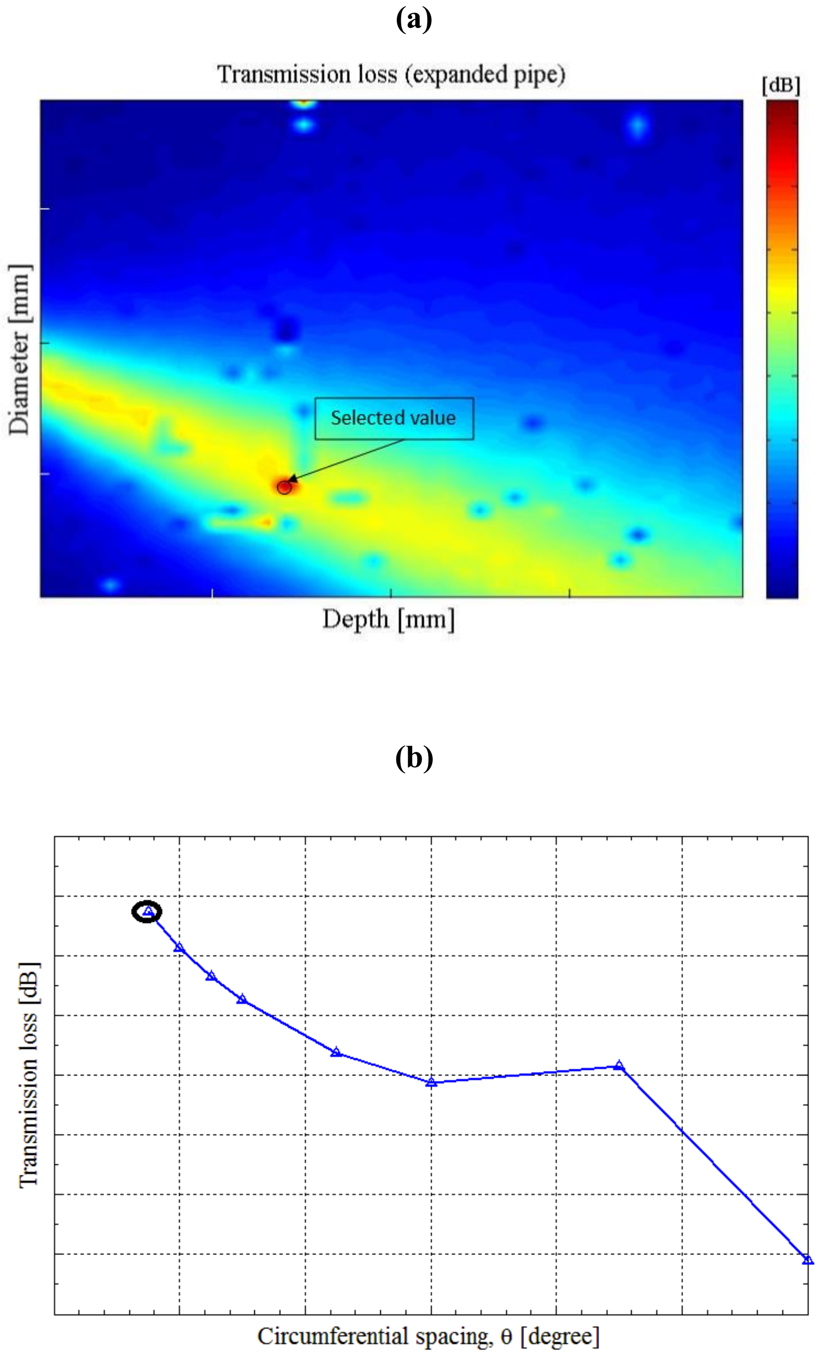

Figure 2.21 TLs of resonators installed on expanded pipe with variations of design parameters: **(a)** Effects of resonator depth and diameter, **(b)** Effects of circumferential spacing, and **(c)** Effects of axial spacing and number of layers

(c)

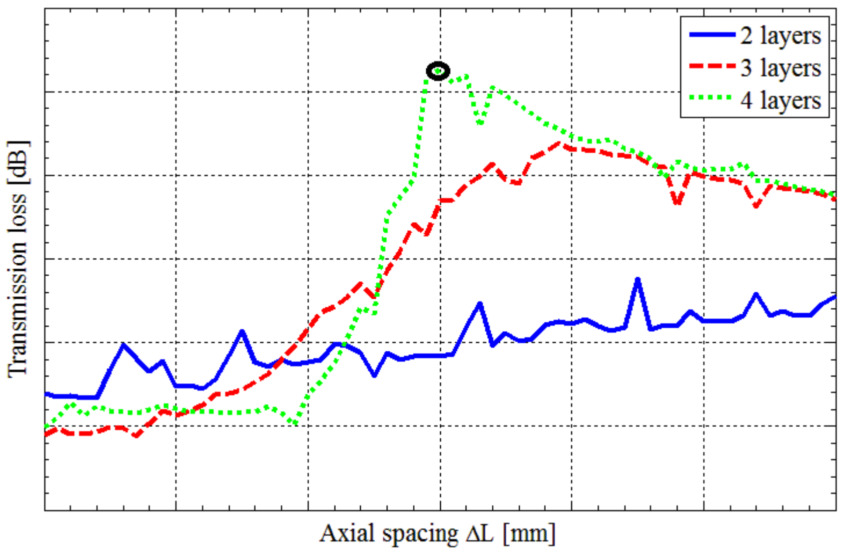

Figure 2.21 Continued

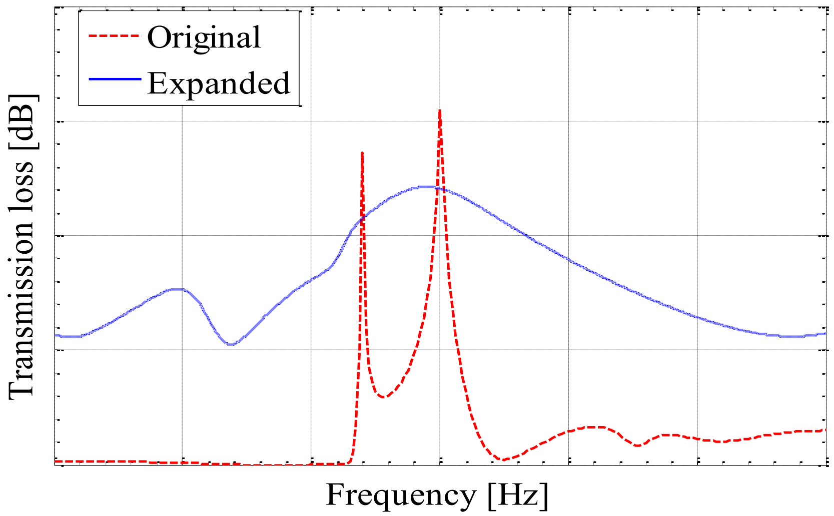

Figure 2.22 TLs of resonators installed on straight and expanded pipes.

CHAPTER III

FLOW EFFECT ANALYSES

3.1 INTRODUCTION

In practical operation process of a centrifugal compressor, the air flow coming out of the compressor are always of temperature higher above room temperature, and of pressures higher than the atmosphere pressure. Also, the Mach number of the air flow at the downstream area can reach to 0.1, or even larger. Thus, from basic thermodynamic theories, it is easy to realize that the speed of sound at the downstream area is changing and is no longer a constant, which results in the non-linearity in the wave equation describing the sound wave propagation [18]. Due to this reason, the performance of the quarter wavelength resonators optimally designed as in the previous chapter may not behave that well as numerical predictions.

In general, there are two aspects needed to be analyzed. First, the working frequency of the resonators may shift away from the target frequency, which is the BPF component of the compressor. The reason of this is due to the non-linearity in the sound speed. In the previous optimal design procedure, it is assumed that the sound speed is a constant of 340 m/s within the finite element domain. Thus, the effective quarter wavelength is no longer exactly the same as expressed in the analytical model as well as the numerical model. From the sensitivity analyses, the performance of the resonators has relatively strict requirement on the geometric dimensions. Hence, even though based on empirical estimations, there will not be large frequency shifts on the resonance frequency, it is still of much importance to investigate the flow effect on the resonator.

Besides the above aspect, another potential factor that will influence the resonators' performance is the aeroacoustic noise coming from turbulent flow. Originally, the air coming out of the compressor is flowing smoothly inside the downstream pipe. But when applying the resonators on the side wall, there are sudden changes in the cross sections of the axial direction. Then the boundary layers are becoming larger after flow passing above the resonator area, and there are vortex generated inside the chamber of the resonator. All of them are the sources of aerodynamic noise. If the design of the resonators bring even more noise that are not negligible, it still cannot be taken into practical applications.

3.2 ACOUSTIC PROPAGATION IN MOVING FLUIDS

Various Industrial problems involve the generation and propagation of acoustic disturbances within a flow. Vehicle pass-by-noise, turbofan noise and exhaust systems are common practical examples. Problem's complexity requires therefore the selection of a set of acceptable assumptions and simplifications. Assuming that the considered fluid is non-viscous and that the flow is adiabatic and irrotational, allows for deriving a continuous potential model. Further decomposition of this velocity potential into a steady-state (mean) flow component and a small acoustic perturbation leads to a convected wave.

3.2.1 Derivation of the flow acoustic model

Based on commonly accepted assumptions, fundamental equations (mass and momentum conservation, and thermodynamic relations) are introduced which, in the context of irrotational flows, reduce to a scalar wave equation involving a velocity potential. The study of acoustic perturbations within a flow [19] is examined through a decomposition of this potential into two components, one related to the ambient flow and the other one related to the acoustic perturbation. The wave equation related to the acoustic perturbation is set up by further linearization of the equation, assuming that acoustic perturbations are small with respect to mean flow quantities.

Assumptions

The flow acoustic problem to be solved refers to the propagation of acoustic sources within a flow. It is assumed that:

1) No heat production due to viscous dissipation occurs in the flow.
2) The fluid is non heat-conducting. No heat transfer occurs in the flow, which is consequently adiabatic.

3) The flow is stationary.
4) Gravity forces are neglected.
5) Fluid elements are in local thermodynamic equilibrium.

The above assumptions also imply that the flow is locally isentropic, that is entropy does not vary locally in time but can vary in space.

3.2.2 Acoustic wave propagation

The acoustic wave correspond to pressure fluctuations which propagate in a non-uniform mean flow. The acoustic solution satisfies the compressible Navier-Stokes equation. In this section, it is introduced a scalar equation for acoustic wave propagation in a non-uniform mean flow.

Continuity equation:

$$\frac{\partial \rho}{\partial t} + \vec{\nabla} \cdot \left(\rho \vec{v} \right) = 0 \tag{3.1}$$

where ρ is the density and ***v*** is the flow velocity.

Momentum equations in Eq. (3.2)

$$\rho \frac{\partial \vec{v}}{\partial t} + \rho \vec{\nabla} \vec{B} = \rho T \vec{\nabla} \vec{s} + \rho \vec{v} \times \left(\vec{\nabla} \times \vec{v} \right) - \vec{\nabla} \vec{\tau} \tag{3.2}$$

where ***B*** denotes the total enthalpy, ***h*** is the fluid enthalpy, **τ** is the viscous stress tensor and ***s*** is the entropy.

Energy equation:

$$\rho \frac{D\vec{B}}{Dt} - \frac{\partial \vec{p}}{\partial t} = \vec{\nabla} \left(\vec{v} \cdot \vec{\tau} \right) + \vec{\nabla} \left(\lambda \vec{\nabla} T \right) \tag{3.3}$$

where *T* is the temperature, and λ is the material's conductivity. Neglecting the power dissipated by viscous stresses and heat conduction leads to

$$\frac{D\vec{B}}{Dt} = \frac{1}{\rho} \frac{\partial \vec{p}}{\partial t} \tag{3.4}$$

which relates the pressure to enthalpy. Combing continuity Eq.(3.1) and simplified energy Eq.(3.4):

$$\frac{\partial \rho}{\partial t} = -\vec{\nabla}\rho\vec{v} = \frac{1}{c^2}\frac{\partial \vec{p}}{\partial t} - \frac{\partial \rho}{\partial s}\frac{\partial \vec{s}}{\partial t} = \frac{\rho}{c^2}\frac{D\vec{B}}{Dt} - \frac{\partial \rho}{\partial s}\frac{\partial \vec{s}}{\partial t} \tag{3.5}$$

By substituting $\rho\frac{\partial \vec{v}}{\partial t}$ with $\frac{\partial}{\partial t}\left(\rho\vec{v}\right) - \vec{v}$, the momentum equation is equivalent to :

$$\frac{\partial \rho\vec{v}}{\partial t} - \frac{\rho\vec{v}}{c^2}\frac{D\vec{B}}{Dt} + \frac{\partial \rho}{\partial s}\vec{v}\frac{\partial \vec{s}}{\partial t} + \rho\vec{\nabla}\vec{B} = \rho T\vec{\nabla}\vec{s} + \rho\vec{v}\times(\vec{\nabla}\times\vec{v}) - \vec{\nabla}\vec{\tau} \tag{3.6}$$

To generalize this formula, two parameters c_T and ρ_T which are the total sound speed and total density fields are introduced, and define a scaled enthalpy ***b*** by equation:

$$\frac{D\vec{b}}{Dt} = \rho_T\frac{D\vec{B}}{Dt} \tag{3.7}$$

This allows to define a parametric momentum equation similar to Eq.(3.6):

$$\begin{aligned} &\frac{1}{\rho_T}\frac{\partial \rho\vec{v}}{\partial t} - \frac{\rho\vec{v}}{\rho_T^2 c^2}\frac{D\vec{b}}{Dt} + \frac{1}{\rho_T}\frac{\partial \rho}{\partial s}\vec{v}\frac{\partial \vec{s}}{\partial t} + \frac{\rho}{\rho_T^2}\vec{\Omega}\vec{b} \\ &= \frac{1}{\rho_T}\left(\rho T\vec{\nabla}\vec{s} + \rho\vec{v}\times\left(\vec{\nabla}\times\vec{v}\right) - \vec{\nabla}\vec{\tau}\right) \end{aligned} \tag{3.8}$$

Up to this point, only the power of viscous stresses and heat released by conduction have been neglected. Combining $\vec{\nabla}\cdot$ Eq.(3.8) and $\frac{\partial}{\partial t}\frac{1}{\rho_T}$ Eq.(3.6) leads to the following equation:

$$\frac{\partial}{\partial t}\left(\frac{\rho}{\rho_T^2 c^2}\frac{D\vec{b}}{Dt}\right) + \vec{\nabla}\left(\frac{\rho\vec{v}}{\rho_T^2}\frac{D\vec{b}}{Dt} - \frac{\rho}{\rho_T^2}\vec{\nabla}\vec{b}\right) = R \tag{3.9}$$

$$\begin{aligned} R = & -\vec{\nabla}\left(\frac{1}{\rho_T}\left(\rho\vec{v}\times\left(\vec{\nabla}\times\vec{v}\right)-\vec{\nabla}\vec{\tau}\right)\right) \\ & +\vec{\nabla}\left(\frac{1}{\rho_T}\left(\frac{\partial\rho}{\partial s}\vec{v}\frac{\partial\vec{s}}{\partial t}-\rho T\vec{\nabla}\vec{s}\right)\right) \\ & +\frac{\partial}{\partial t}\left(\frac{1}{\rho_T}\frac{\partial\rho}{\partial s}\frac{\partial\vec{s}}{\partial t}+\rho\vec{v}\frac{1}{\rho_T}\right) \end{aligned} \tag{3.10}$$

This equation is directly derived from the compressible Navier-Stokes equations and is valid for the flow and the acoustic part. The acoustic quantities are generally well defined by a harmonic expansion (Fourier transform):

$$q(x,t)=\sum_{\omega}q(x,\omega)e^{i\omega t}=\sum_{\omega}\mathscr{F}\left(q(x,t)\right)e^{i\omega t} \tag{3.11}$$

Applying the Fourier transform to Eq.(3.9) leads to

$$\begin{aligned} & \sum_{\omega}\frac{i\omega\rho_0}{\rho_T^2c^2}\left(i\omega b+v_0\cdot\vec{\nabla}b\right)e^{i\omega t} \\ & +\sum_{\omega}\vec{\nabla}\left(\frac{\rho_0 v_0}{\rho_T^2c^2}\left(i\omega b+v_0\cdot\vec{\nabla}b\right)-\frac{\rho_0}{\rho_T^2}\vec{\nabla}b\right)e^{i\omega t}=\sum_{\omega}R\cdot e^{i\omega t} \end{aligned} \tag{3.12}$$

The harmonic functions $e^{i\omega t}$ represent a set of orthogonal functions, which means that the sum of equations will be satisfied only if each equation is satisfied:

$$\begin{aligned} & -\frac{\omega^2\rho_0}{\rho_T^2c^2}b+\frac{i\omega\rho_0}{\rho_T^2c^2}v_0\cdot\vec{\nabla}b+\vec{\nabla}\cdot\left(\frac{i\omega\rho_0v_0}{\rho_T^2c^2}b+\frac{\rho_0v_0}{\rho_T^2c_0}v_0\cdot\vec{\nabla}b-\frac{\rho_0}{\rho_T^2}\vec{\nabla}b\right)=R \\ & R=-\vec{\nabla}\cdot\frac{1}{\rho_T}\mathscr{F}\left(\rho v\times\left(\vec{\nabla}\times\vec{v}\right)-\vec{\nabla}\tau\right) \\ & +\vec{\nabla}\cdot\frac{1}{\rho_T}\mathscr{F}\left(\frac{\partial\rho}{\partial s}v\frac{\partial s}{\partial t}-\rho T\vec{\nabla}s\right)+i\omega\mathscr{F}\left(\frac{\partial\rho}{\partial s}\frac{\partial s}{\partial t}+\rho v\cdot\vec{\nabla}\frac{1}{\rho_T}\right) \end{aligned} \tag{3.13}$$

The left hand side of Eq.(3.13) corresponds to the acoustic wave operator in a non-uniform mean flow for the acoustics field represented by enthalpy fluctuations b. A strategy originally proposed by Lighthill [8], Möhring [20] shows that the right hand side *R* corresponds to flow fluctuations which are considered as acoustic sources. The right hand side can be computed using unsteady CFD results. This corresponds to the analogies described in the introduction section.

3.2.3 Acoustic propagation in a medium at rest

This section corresponds to the case where $v_0 = 0$. In this case, the material derivative D/D*t* is similar to time derivative $D/Dt = \partial/\partial t$ and Eq. (3.13)becomes:

$$-\frac{\omega^2 \rho_0}{\rho_T^2 c^2} b - \vec{\nabla} \cdot \left(\frac{\rho_0}{\rho_T^2} \vec{\nabla} b \right) = R \tag{3.14}$$

Using Eq. (3.4) which related pressure to total enthalpy, and using the fact that $\rho_T = \rho_0$ when $v_0 = 0$, the above equation becomes:

$$-\frac{\omega^2}{\rho_0 c^2} p - \vec{\nabla} \left(\frac{1}{\rho_0} \vec{\nabla} p \right) = R \tag{3.15}$$

which is the Fourier transform of the following equation which is valid for acoustic waves propagation in a inhomogeneous medium at rest:

$$\frac{\partial}{\partial t} \left(\frac{1}{\rho_0 c^2} \frac{\partial p}{\partial t} \right) - \vec{\nabla} \left(\frac{1}{\rho_0} \vec{\nabla} p \right) = 0 \tag{3.16}$$

3.2.4 Acoustic propagation in a potential flow

If it is assumed the flow is entropic, irrotational and neglect viscous stresses, Eq. (3.2) reduce to:

$$\rho \frac{\partial v}{\partial t} = -\rho \vec{\nabla} B \tag{3.17}$$

The Fourier transform equivalent is

$$i\omega \rho_0 v = -\rho_0 \vec{\nabla} B \tag{3.18}$$

the enthalpy fluctuations are similar to a velocity potential ϕ:

$$i\omega \phi = B \tag{3.19}$$

Introducing Eq. (3.19) into Eq. (3.14) and using the fact that ρ_T is constant through space in an isentropic flow, it is obtained:

$$-\frac{\omega^2\rho_0}{\rho_T^2c^2}\left(i\omega\phi+v_0\vec{\nabla}\phi\right)+i\omega\left(\vec{\nabla}\left(\frac{\rho_0 v_0}{\rho_T^2c^2}\left(i\omega\phi+v_0\vec{\nabla}\phi\right)-\frac{\rho_0}{\rho_T^2}\vec{\nabla}\phi\right)\right)=0 \tag{3.20}$$

Integrating with respect to time, it is derived:

$$\frac{i\omega\rho_0}{\rho_T^2c^2}\left(i\omega\phi+v_0\vec{\nabla}\phi\right)+\vec{\nabla}\left(\frac{\rho_0 v_0}{\rho_T^2c_2}\left(i\omega\phi+v_0\vec{\nabla}\phi\right)-\frac{\rho_0}{\rho_T^2}\vec{\nabla}\phi\right)=0. \tag{3.21}$$

which is the classical convected acoustic equation for velocity potential.

3.3 LIGHTHILL'S ACOUSTIC ANALOGY

In this section, the fundamental equation describing the Lighthill's acoustics analogy is introduced. The Lighthill's analogy [8] is the theoretical basis for the application of hybrid method in this study.

For a compressible fluid, the mass conservation (continuity) equation can be written, using index notation, as:

$$\frac{\partial\rho}{\partial t}+\frac{\partial\rho v_i}{\partial x_i}=0 \tag{3.22}$$

where ρ is the fluid density and v_i is the fluid velocity vector. The momentum conservation equation can be written:

$$\frac{\partial\rho v_i}{\partial t}+\frac{\partial\rho v_i v_j}{\partial x_j}=-\frac{\partial p_{ij}}{\partial x_j} \tag{3.23}$$

where p_{ij} is the compressive stress tensor. This last equation is rewritten by adding a new term to both sides, a_0 being a constant which can be chosen arbitrarily at this stage:

$$\frac{\partial\rho v_i}{\partial t}+a_0^2\frac{\partial\rho}{\partial x_i}=-\frac{\partial T_{ij}}{\partial x_j} \tag{3.24}$$

where the tensor T_{ij} is defined by:

$$T_{ij} = \rho v_i v_j + p_{ij} - a_0^2 \rho \delta_{ij} \tag{3.25}$$

For a Stokesian perfect gas such as air, the compressive stress tensor p_{ij} can be reformulated as:

$$p_{ij} = p\delta_{ij} + \tau_{ij} \tag{3.26}$$

where p is the pressure and τ_{ij} is the viscous stress tensor. The expression of T_{ij} then becomes:

$$T_{ij} = \rho v_i v_j + \delta_{ij}(p - a_0^2 \rho) + \tau_{ij} \tag{3.27}$$

Now a_0 is chosen to be the speed of sound in a uniform medium at rest $a_0 = c$. For a Stokesian perfect gas such as air c is given by the following relation:

$$a_0^2 = c^2 = \left(\frac{\partial p}{\partial \rho} \right)_s = \frac{\gamma p}{\rho} \tag{3.28}$$

where γ is the ratio of specific heats.

For a Stokesian perfect gas like air, in an isentropic, high Reynolds number and low Mach number flow, Lighthill's tensor [16] T_{ij} is often approximated by:

$$T_{ij} \approx \rho v_i v_j \tag{3.29}$$

This also shows that if the aeroacoustic sources are computed from incompressible CFD results (density is constant in time), only flow velocity results are needed.

3.4 COMPUTATION FLUID DYNAMIC SIMULATION

3.4.1 Introduction

It has been a long time since the establishment of the science of computation fluid dynamics and the practical application of that science. The governing equation for Newtonian fluid dynamic is the unsteady Navier-Stokes equations, which has been known for 150 years or more. In order to solve these equations and analyze fluid dynamic problems, scientists and engineers have developed many reduced form of these equations, and its development is still an active area of research nowadays.

Traditionally, in solving fluid dynamics problems, engineers took advantages of experimental ways a lot, of which one widely known example is the wind tunnel. Wind tunnel experiment has been an effective ways for simulating real flows. It provides a cost-effective alternative to the full-scale measurement. However, for large scale measurement like in the design of aircraft, experimental fluid dynamics still has limitations.

As the rapid development of computer technologies and memory sizes since the 1950s, computational fluid dynamics (CFD) techniques [21] has been brought into academic as well as industrial uses. Due to the cheap cost of CFD compared to experimental fluid dynamics methods, it is becoming a more and more popular technique in solving fluid dynamics problems. Also, those problems with high Reynolds numbers, which cannot be solved by using experimental fluid dynamics methods, can be easily simulated with the application of CFD.

3.4.2 Discretization Method

One of the most important issues during the process of applying CFD in solving fluid dynamics problems is the discretization of partial differential equations (PDE). There are a number of methods to discretize PDEs, e.g, finite difference method, finite volume method and finite element method. The choice of discretization methods depends on whether time derivative or only spatial derivative are considered. In other words, it is needed to specify whether or not the PDE is time dependent. In time dependent problems, the discretization method is exclusively the finite difference methods. In problems with only spatial derivatives, the methods of finite volume as well as finite element can be used. Besides that, the stability and consistency of the different methods are needed to be considered in the choice of discretization methods.

Finite Volume Method

Finite volume method is the most commonly used method in spatial discretization in CFD. 'Finite volume' is the volume space around each node on a mesh element. The method is realized by taking the integrals along the element boundaries. Then the flux going through the element is evaluated. And the flux entering the element is identical to that leaving the adjacent element. Another advantage of finite volume method is that it can be easily used for the construction of unstructured mesh.

Finite Difference Method

Finite difference method is used in the discretization in spatial domain as well as in time domain. It is realized by using the Taylor series expansion on each term of the PDEs. There are numbers of schemes of applying finite difference method in the discretization in space and time domains, e.g., FTCS (Forward time centered space) scheme, DuFort-Frankel scheme, Crank-Nicolson scheme and etc [21]. For each scheme, the stability and accuracy requirements are different. Both the time step size and the element size in space domain determine the accuracy and the stability of the results by using each of the schemes.

Finite Element Method

Finite element method is the most widely used method in structural mechanics. However, in solving CFD problems, finite element method can still be taken into application in the discretization of space domain. When using finite element method, it is required special cares on the formulation of finite element, so that the solutions can be conservative. Besides that, finite element method is more stable than the finite volume approach [21].

3.4.3 Turbulence Models

Another important issue in CFD simulation is the choice of turbulence models. In order to solve problems with different kinds of turbulence flows, it is of much important to choose the most proper turbulence model, so that the accuracy of the simulation results is guaranteed and the computation time is minimized.

***k*- *ε* Model**

The *k*- *ε* model is the most widely used method for industrial applications due to its better convergence rate and lower memory requirements. The *k*- *ε* turbulence model was first introduced by Kolmogorov in 1942 [22]. In general, it solves for two variables: the turbulent kinetic energy, *k*, and the rate of dissipation of kinetic energy, *ε*. *k*- *ε* model is working well for simulating external flow problems around complex geometries. However, it is not capable of computing very accurately for flow fields that exhibit adverse pressure gradients or jet flow.

***k*- *ω* Model**

The *k*- *ω* model is another semi-empirical method similar to *k*- *ε*. In *k*- *ω* turbulence model, besides the turbulent kinetic energy *k*, it solves for the specific rate of dissipation of kinetic energy, *ω*. It also uses wall functions and therefore it does not have big memory requirements. It is more difficult to converge and is very sensitive to solution initialization. Hence, the *k*- *ε* model is often used as an initial condition for solving the *k*- *ω* model. The *k*- *ω* model is more powerful in the situations where the k- *ε* model cannot obtain accurate solutions, such as internal flows, separated flows, and jets [22].

LES Model

Large eddy simulation (LES) is another popular technique for turbulence flow simulations. The principal operation in large eddy simulation is low-pass filtering. It is applied to the Navier-Stokes equation by directly solving large scale motions and approximating small scales of motions. LES is a computationally efficient method widely used in academia field, including combustion, acoustics, and simulations of the atmospheric boundary layer.

One limitation of the LES method is that it requires extremely fine mesh near the boundary wall region. In other words, LES method is not recommended for flow with large wall boundary layers. Another limitation is that LES has relatively higher stability requirements. Therefore, it requires long computational time to reach a stable state for running LES model.

3.5 CFD SIMULATION

3.5.1 Pre-Processing

The CFD simulations are performed by using commercial software ANSYS FLUENT, which is one of the most widely used packages for solving CFD problems. In the pre-processing steps, a CAD model is built by using commercial software (i.e., Solidworks) with the geometric parameters obtained from the optimal design procedures. The CAD model is then imported into ANSYS for CFD computations. Regarding to meshes, it is generated automatically using the built-in module in ANSYS. The unstructured meshes are generated, and the linear tetrahedron element is used. The maximum element size is as 5 mm with prism layers near the wall boundaries where there are more turbulences. By doing so, the Courant-Friedrichs-Lewy (CFL) stability condition requirement in CFD can be satisfied. The Courant number is defined as

$$c = u\frac{\Delta t}{\Delta x} \tag{3.30}$$

where u is the flow speed, Δt is the time step size and Δx is the element size. The schematic of the mesh is shown in Figure 3.1,

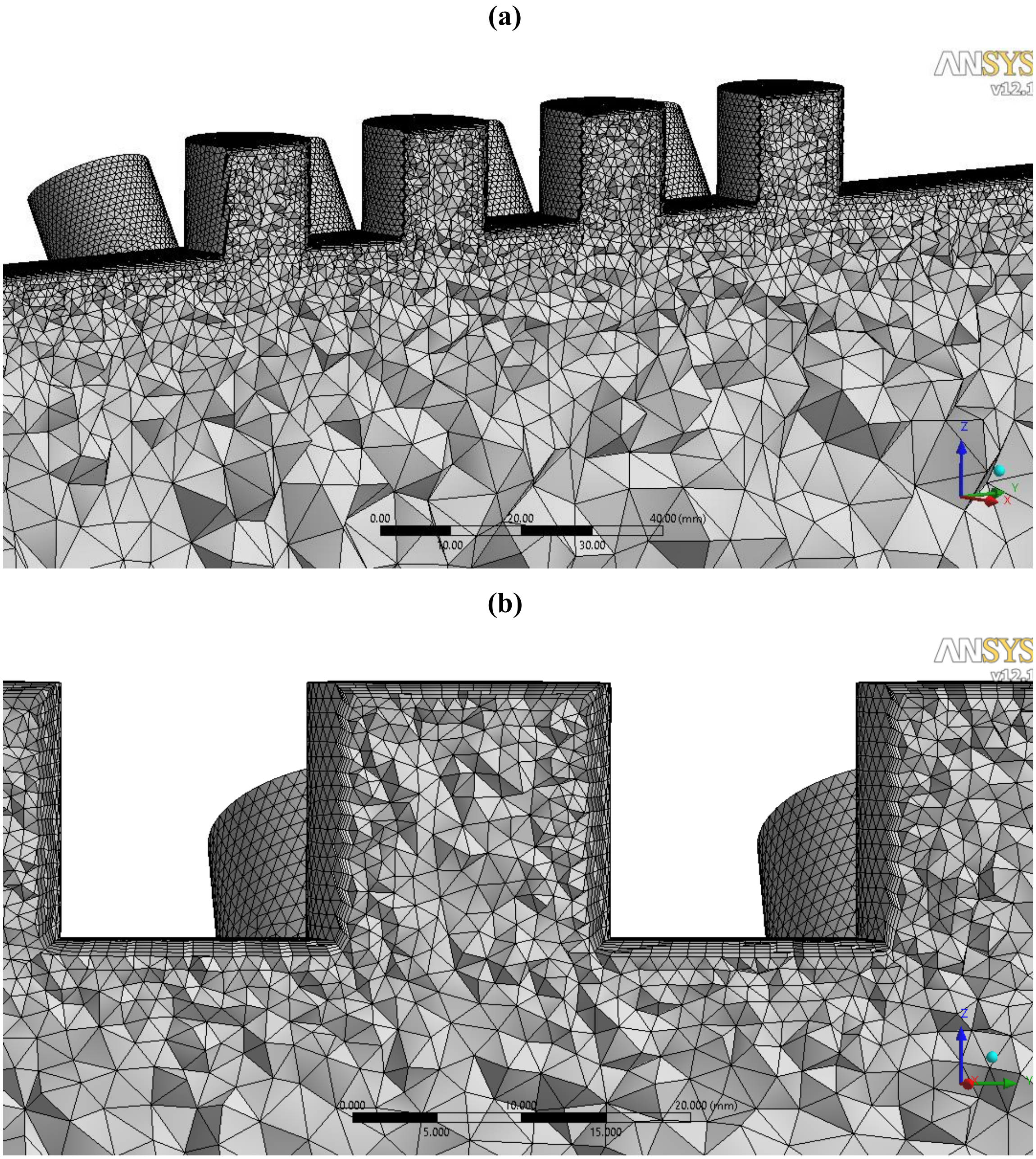

Figure 3.1 (a) Overall mesh and **(b)** boundary mesh with prism layers.

3.5.2 Steady-State Simulation

A steady-state simulation is performed first to obtain the flow domain solution for mean flow effect analyses in aeroacoustic simulations. Besides that, the steady-state results can be used for the initialization of the transient state simulation. It is well known that it takes a long time form the transient state simulation to converge. However, since the steady-state solution is already converged, it will largely decrease the iteration numbers in each time step in transient simulations.

In steady-state simulation, the realizable *k*-epsilon turbulence model is used. The term "realizable" means that the model satisfies certain mathematical constraints on the Reynolds stresses. For near-wall treatment, the non-equilibrium wall functions is selected. The inlet boundary is set as velocity inlet, with flow speed of 21 m/s and 0.01% turbulent intensity. The outlet boundary is set as pressure outlet, with 0 Pa gauge pressure, which means that the outlet pressure is equivalent to atmosphere pressure.

Regarding to pressure-velocity coupling, the SIMPLE (semi-implicit method for pressure-linked equations) method is selected. The least squares cell based gradient method is chosen for its better performance with unstructured meshes. Besides that, the second-order upwind scheme is used in the spatial discretization. The simulation is initialized from the inlet.

Table 3.1 Steady-state simulation setup in ANSYS FLUENT

Turbulence Model	Realizable *k*-epsilon model
Inlet Boundary	Velocity inlet, 21m/s
Outlet Boundary	Pressure outlet, Gauge pressure $P = 0$ Pa (1 atm)
Pressure-Velocity Coupling	SIMPLE
Spatial Discretization	Second-order Upwind Scheme
Solution Initialization	Compute from Inlet

After about 320 iterations, the results are converged. The plot of the residuals are shown in Figure 3.2. The convergence criteria is set as 1×10^{-3} for the variables of velocity, continuity and etc. Figure 3.3 shows the velocity contours results colored by velocity magnitude. From the simulation results, it can be seen that the flow speed inside the pipe does not change much, and the flow inside the resonators are of very low speed. Also, after flow going pass the resonator areas, the turbulence boundary layers near the wall become larger.

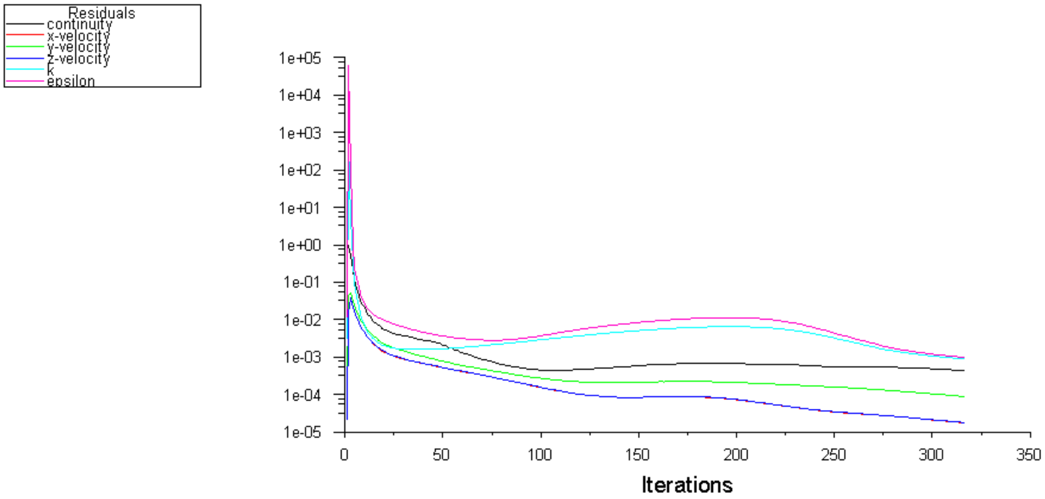

Figure 3.2 Plot of residuals of steady-state CFD simulation.

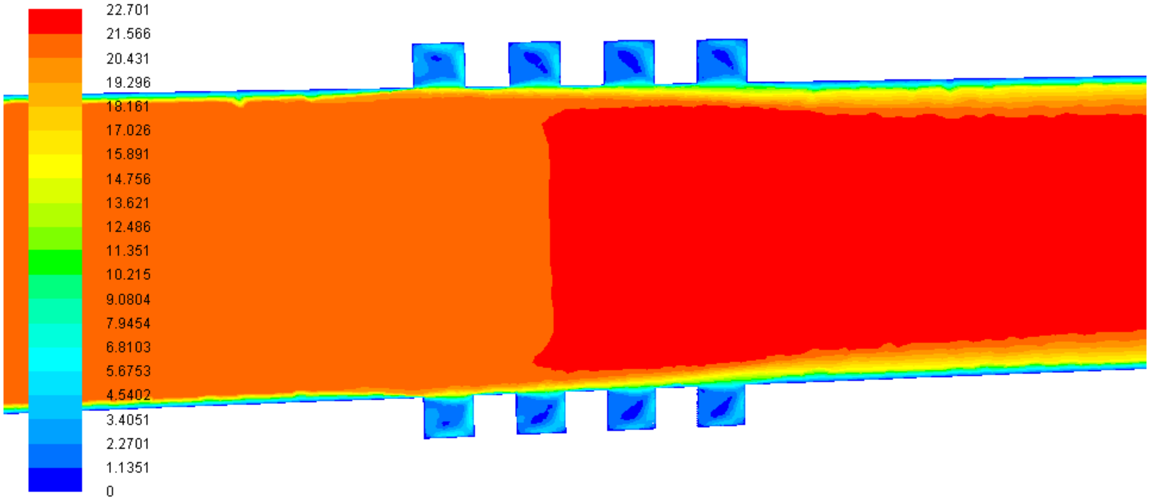

Figure 3.3 Cut-plane view of velocity contours colored by velocity magnitude.

3.5.3 Transient Simulation

In order to analyze the aerodynamic noise generated from the turbulent flow, a transient simulation is needed to be conducted. The initialization of transient simulation can be achieved by using the results from steady-state simulation, so that it spends less time for the convergence of the results in each time step. The time step size, Δt is set as 1×10^{-4} second, and the number of time steps saved, N is 2000. Then the maximum frequency, f_{max} and the resolution of frequency, Δf after Discrete Fourier Transform (DFT) in later aeroacoustic simulation can be calculated by as 5000 Hz from 5 Hz, respectively. The calculation of maximum frequency and frequency resolutions are obtained from the following equations,

$$f_{\max} = 1/2\Delta t \tag{3.31}$$

$$\Delta f = 1/\left(N\Delta t\right) \tag{3.32}$$

Notice that the term $1/\Delta t$ equals to the sampling frequency, and the maximum frequency is calculated by taking the half of the sampling frequency to satisfy the Nyquist sampling criterion. The simulation setup for transient simulation are shown in Table 3.2.

Table 3.2 Transient simulation setup in ANSYS FLUENT

Turbulence Model	Large Eddy Simulation (LES) model
Inlet Boundary	Velocity inlet, U = 21m/s
Outlet Boundary	Pressure outlet, Gauge pressure P = 0 Pa (1 atm)
Pressure-Velocity Coupling	SIMPLE
Spatial Discretization	Second-order Upwind Scheme
Time Domain Discretization	Second-order Implicity
Gradient Method	Least Squares Cell Based
Solution Initialization	Compute from Steady-state results
Time step size	0.0001 s
Number of time step saved	2000

The result of turbulent intensity is shown in Figure 3.4. It can be seen that the turbulent intensities are larger around the corner of the resonators. Thus, it can be estimated that there will be more aerodynamic noise generated from that area.

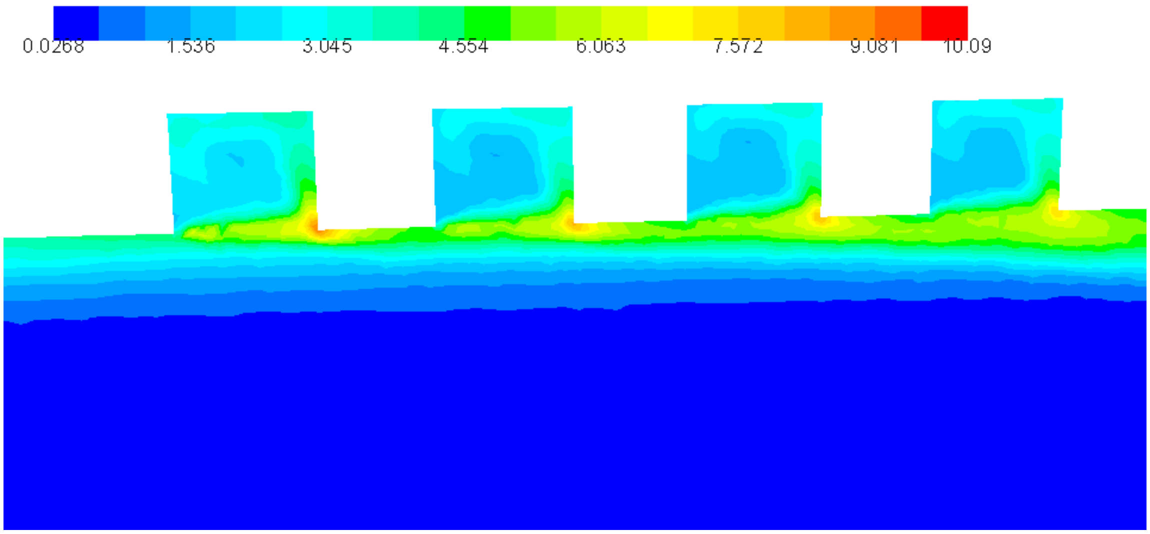

Figure 3.4 Cut-plane view of contours of turbulent intensity (%) at 0.001 seconds.

3.6 MEAN FLOW EFFECT

3.6.1 Transferring CFD Results

In order to analyze the mean flow effect on the performance of the quarter wavelength resonators, the CFD solutions are imported into acoustic FEM software (i.e., ACTRAN), and mapped onto the acoustic meshes. The mapping is realized by employing the iCFD utility, which is an interface between CFD codes and ACTRAN. Besides that, the iCFD utility can also be used for computation of aeroacoustic sources and Fourier transform of time domain quantities. They are shown in the next section analyzing the aerodynamic noise.

There are two methods provide by the iCFD utility about the mapping from CFD solutions to acoustics mesh, (1) linear interpolation and (2) conservative integration. The schematics showing the two methods are in Figure 3.5 and Figure 3.6, respectively. From that, it can be seen the acoustic meshes can be coarser than the CFD meshes. From Figure 3.5, it can be seen that by using linear interpolation method, some of the information will be loss due the inconsistency of the meshes. However, the conservative integration method as shown in Figure 3.6 is capable of preserving all CFD information. Thus, the conservative integration method is used when transferring CFD solutions to acoustics domain.

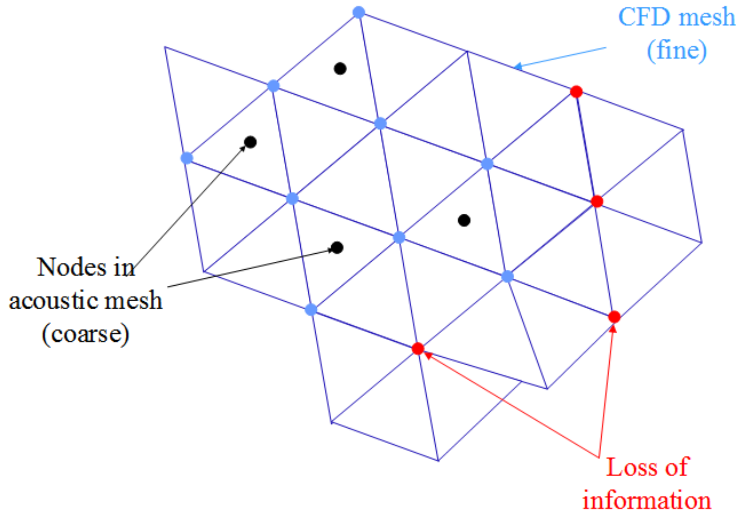

Figure 3.5 Linear interpolation from CFD mesh to acoustic mesh.

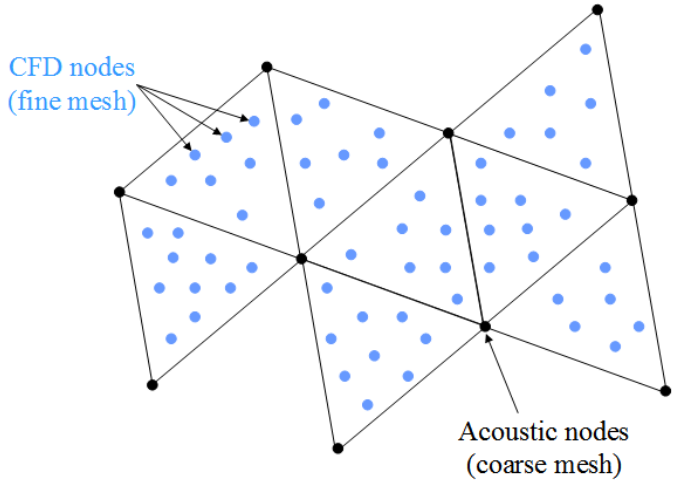

Figure 3.6 Conservative integration from CFD mesh to acoustic mesh.

3.6.2 Frequency Shifts

After CFD simulations, the steady-state solutions are first used to analyze the mean flow effect on the performance of the quarter wavelength resonators. In order to estimate the relation between how much frequency shifts and the Mach number of flow, several cases with different flow speed are simulated. In the aeroacoustic simulations, the boundary conditions are identical to those as previously set in the optimal design procedures, a plane wave excitation is given at the inlet boundary. However, in the following chapter of experimental validation, the excitation is set as random waves, with higher mode waves in the axial direction as well as the circumferential direction, in order to simulate the real experiment condition. Besides that, the mean flow field obtained from CFD simulations is mapped onto the acoustic domain. The simulation result is shown in Figure 3.7. It can be seen that as the increase of flow speed, the resonance peaks are shifted toward lower frequencies. Also, the magnitude of the TL at the second peak is reduced as flow speed becomes faster.

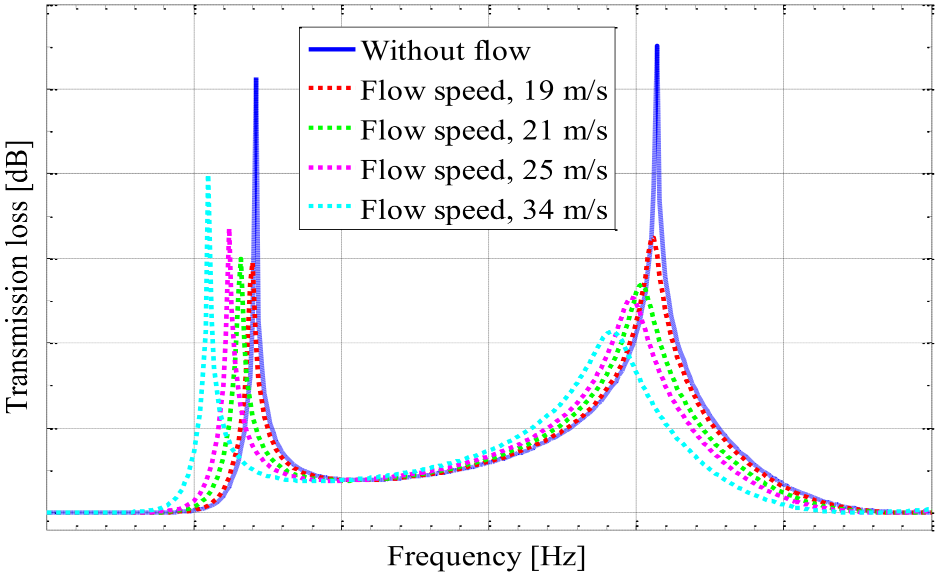

Figure 3.7 Plot of transmission losses at various flow speed.

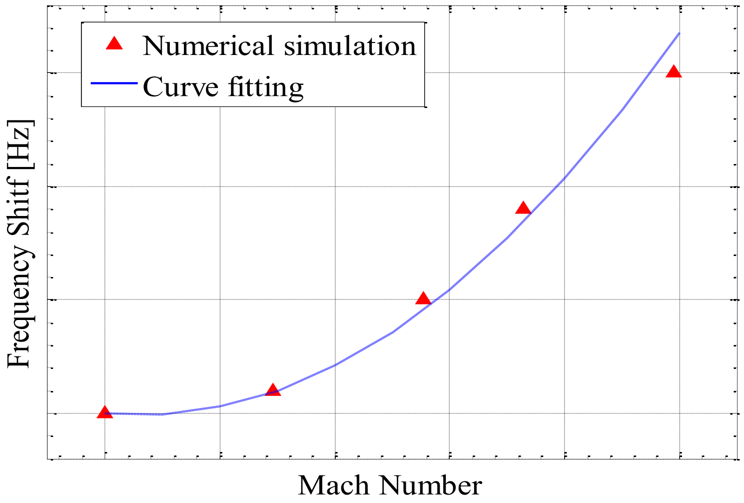

Figure 3.8 Frequency shift at 2nd resonance peak versus Mach numbers.

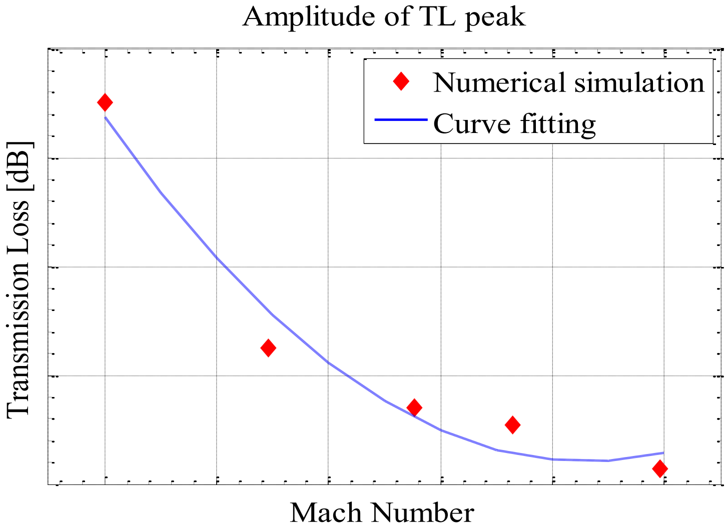

Figure 3.9 Amplitudes of TL at 2nd resonance peak versus Mach numbers.

Figure 3.8 shows the relationships between frequency shifts and Mach numbers. The second order polynomial is well fitted to the frequency shift, indicating that the frequency shift is proportional to the square of the Mach number (i.e., $\Delta f = 1918.16M^2 - 24.21M$). The relationships between the amplitudes of TLs at the 2nd resonance peak is shown in Figure 3.9, also with a second order polynomial fitted curve. These relations can be taken as a reference in the design of the quarter wavelength resonators in the future.

3.7 EXPERIMENTAL VALIDATION OF MEAN FLOW EFFECT

3.7.1 Experimental Setup

As shown in Figure 3.10, the test rig for experimental validation includes a pipe system with the resonators, a loudspeaker system including a power amplifier, reference microphones, a hologram microphone array, a National Instruments (NI) data acquisition (DAQ) system, a signal generator (not shown in the figure), and an air blower (not shown in the figure). The coaxial, two-way loudspeaker (model: JBL DRVN) is driven by a random excitation signal up to 6.4 kHz generated by the signal generator through the power amplifier. The four reference microphones (model: Brüel & Kjær Type 4954A) are flush mounted on the inner wall of the pipe with the sampling interval of 90^o in the θ-direction (i.e., circumferential direction) close to the loudspeaker. The loudspeaker input signal is also recorded as a reference signal. The reference signals measured by using the reference microphones are used to reduce the effects of background noise using a partial field decomposition technique as well as to synchronize two array measurements at the upstream and downstream of the resonators. The hologram microphone array of 8×8 microphones (model: Brüel & Kjær Type 4958) are flush mounted inside along the pipe with the sampling spacing of $\Delta z = 0.025$m and $\Delta\theta = 45^o$. The hologram microphone array is placed at either the upstream or the downstream of the resonator array to reconstruct the acoustic fields at these two measurement locations. The DAQ system that consists of a NI PXIe-1082 chassis and five NI PXIe-4496 modules are used to record both the reference and the hologram microphone signals. During measurement, the sampling frequency is set to 16384 Hz so that the maximum frequency of the recorded data can be 8192 Hz. However, since the maximum frequency determined from the sampling interval in the *z*-direction (i.e., Δz = 0.025m) is approximately 6.4 kHz with the sound speed of 340 m/s, the resulting maximum frequency should be determined as 6.4 kHz.

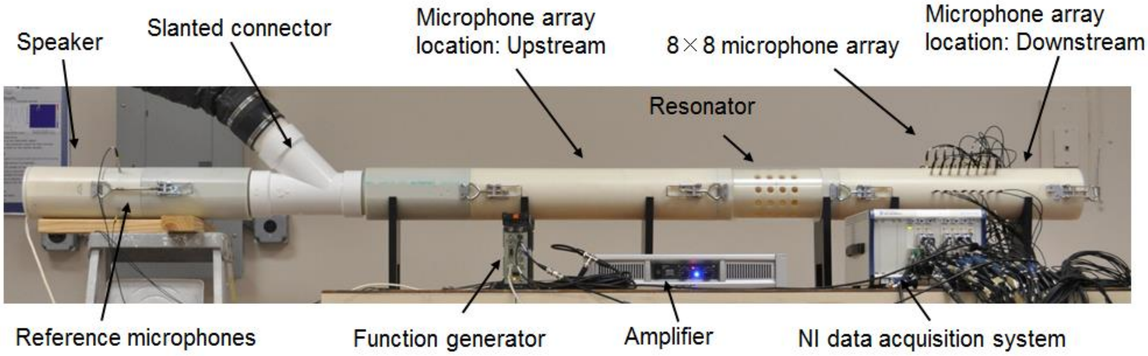

Figure 3.10 In-lab test rig for validation of numerical flow effect analyses.

In order to experimentally validate the effect of the airflow inside the pipe on the performance of the resonators, the spatially averaged airflow speed of 21m/s (i.e., Mach Number = 0.06) is generated by the blower and the airflow is then injected into the pipe through the slanted Y connector as shown in Figure 3.10.

3.7.2 In-lab Test Results

Figure 3.11(a) shows the incident and the transmitted acoustic powers measured from the experiments by using near-field acoustic holography (NAH) [23] method without airflow and Figure 3.11(b) shows the TL obtained from the difference of the incident and the transmitted acoustic powers in.

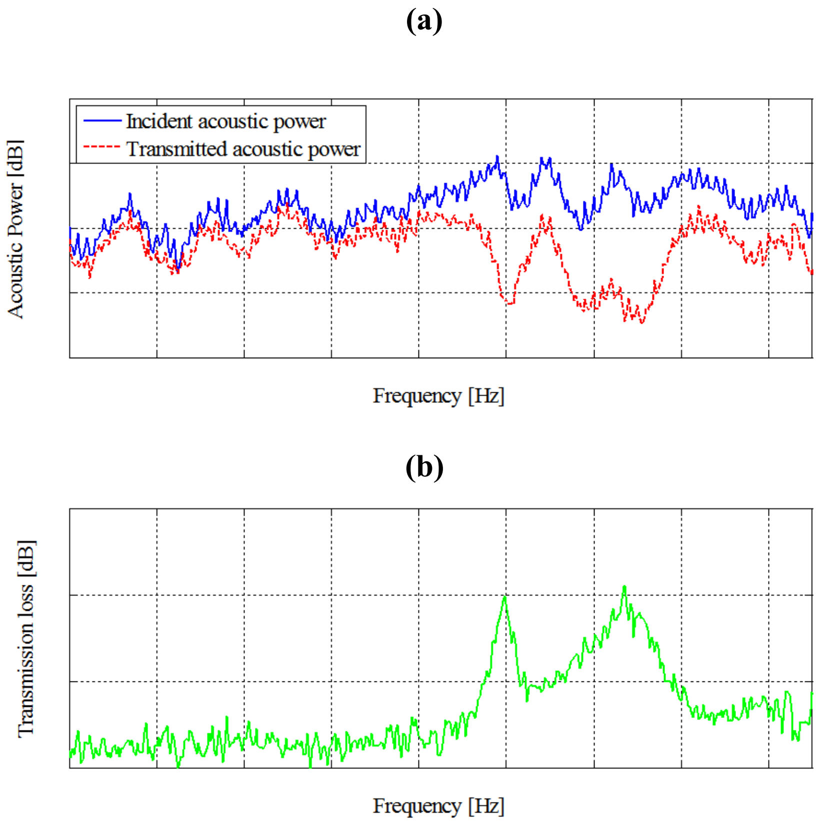

Figure 3.11 **(a)** Measured incident and transmitted acoustic powers and **(b)** TL calculated from measured acoustic powers.

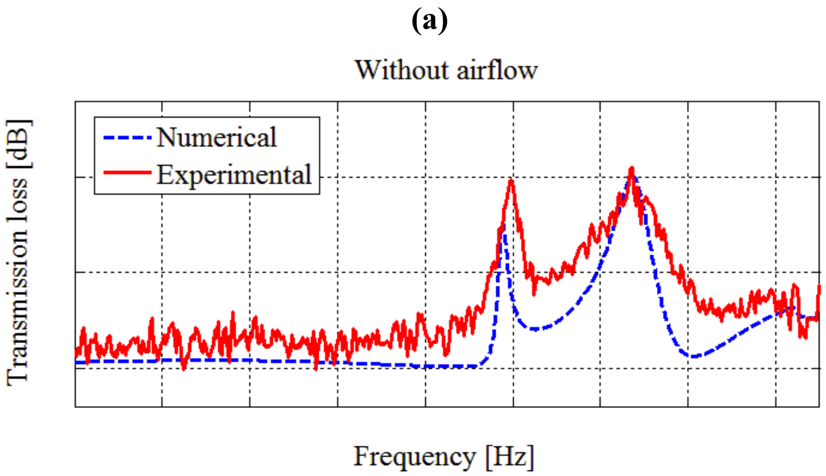

Figure 3.12 Predicted and measured TL **(a)** without airflow and **(b)** with airflow.

(b)

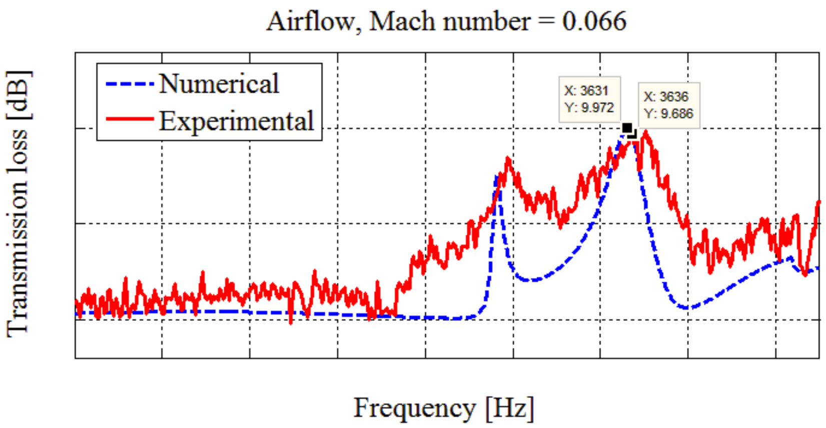
Airflow, Mach number = 0.066

Figure 3.12 Continued

Figure 3.12 shows the comparison between predicted and experimentally measured TL with and without airflow. The measured and predicted TL agree well with each other in terms of the maximum peak locations and amplitudes with the maximum frequency difference of 10 Hz. As for the predicted results, there are the frequency shifts of 6 Hz due to the airflow inside the pipe, which may be negligibly small. However, the frequency shifts in the experimental results are approximately 0 - 5 Hz, even though they are not clearly identified due to measurement noises. On the other hand, the slanted connector and the curvature of the resonator end that are not modeled in the numerical model may have some effects on the TL results, although they do not cause any significant TL discrepancies between the experimental and numerical results. In addition, the discrepancies may be caused by the resonator’s machining errors. The background noise in the experimental facility and the wave reflections from the ground and the walls of the experimental facility may also contribute to the discrepancies.

3.8 AEROACOUSTIC NOISE

3.8.1 Numerical Prediction

The simulations of investigating the aeroacoustic noise generated from the turbulent flow inside the pipe system with quarter-wavelength resonators are performed by using ACTRAN with the unsteady CFD solution data obtained from the previous steps. The time data from CFD solution are transformed into frequency domain by DFT using the iCFD module in ACTRAN.

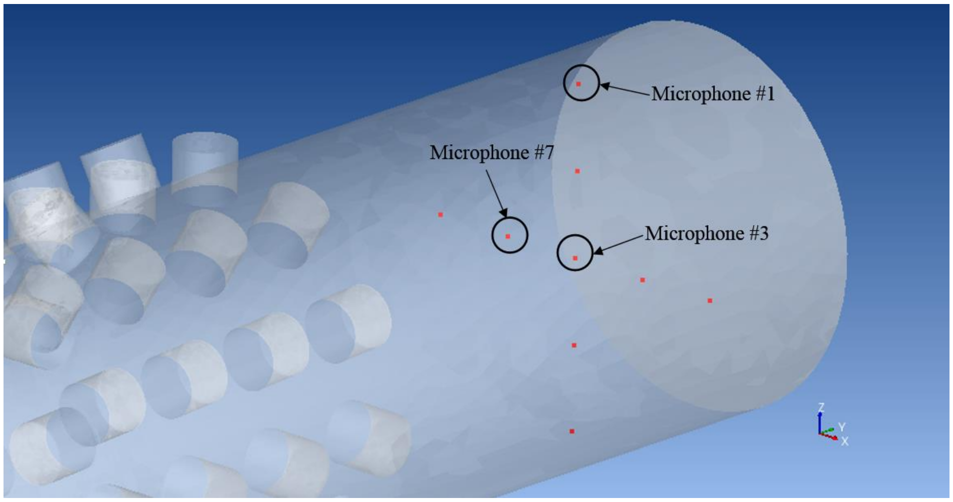

Figure 3.13 Microphone locations in simulation of aeroacoustic noise.

Figure 3.**13** shows the microphone locations in aeroacoustic simulations. In total, 9 microphone points are set at the downstream area. Aeroacoustic noise generated from the turbulence flow are evaluated at all of the measuring points. The noise at microphone 1, microphone 3 and microphone 7 are shown in Figure 3.14(a), Figure 3.14(b) and Figure 3.14(c), respectively. From that, it can be seen that the maximum noise level is less than 60 dB, which can be ignored when compared with the overall noise level.

(a)

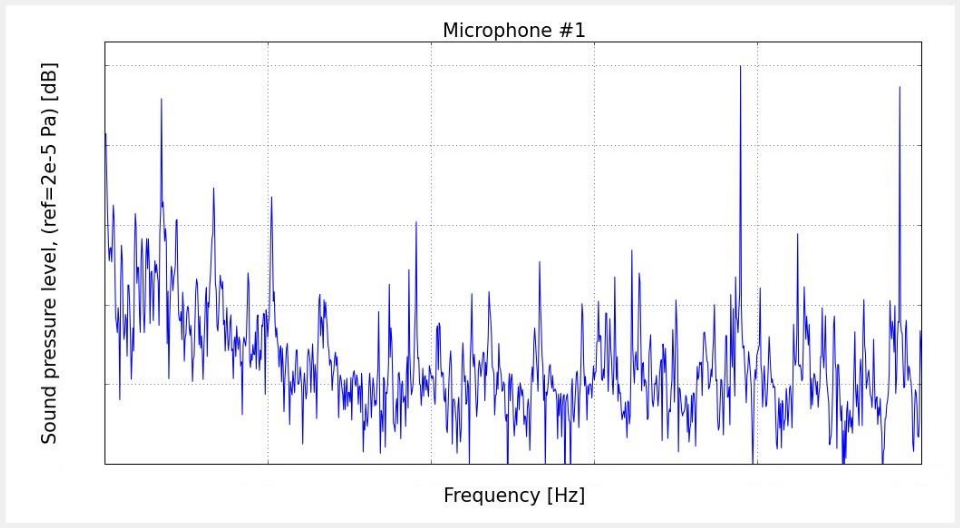

(b)

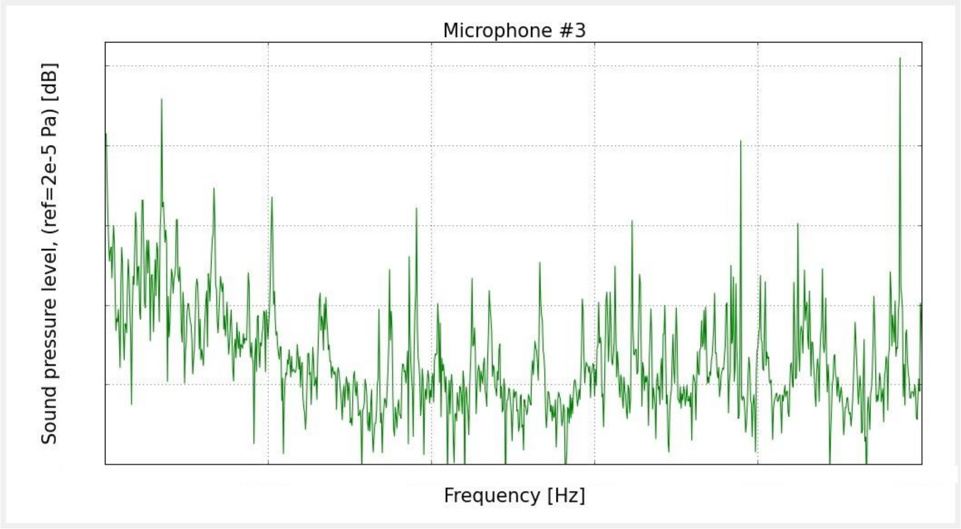

Figure 3.14 Aeroacoustic noise from **(a)** microphone 1, **(b)** microphone 3 and **(c)** microphone 7.

(c)

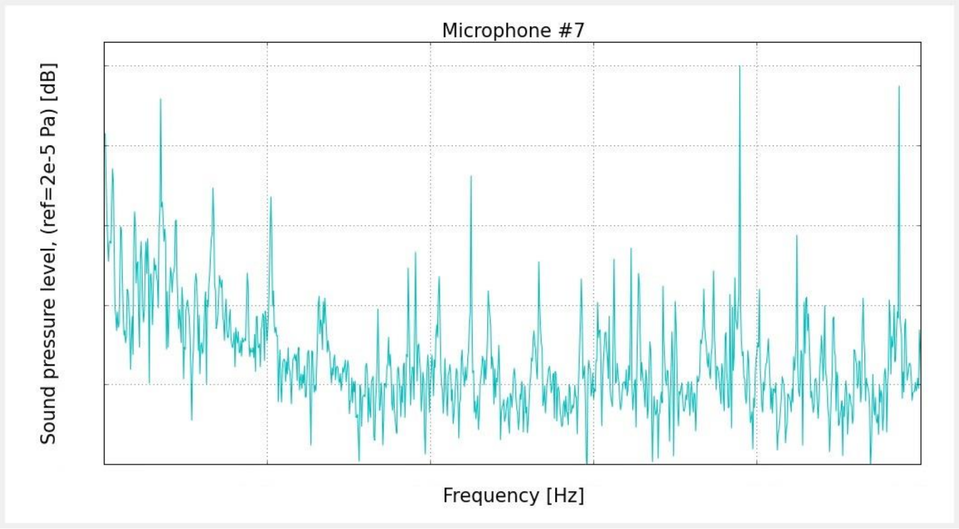

Figure 3.14 Continued

CHAPTER IV

CONCLUSIONS AND FUTURE WORKS

In order to reduce the tonal noise generated from a centrifugal compressor, the quarter wavelength resonator array is proposed and has been studied in this thesis. The quarter wavelength resonator array is installed at the downstream area of a compressor for tonal noise reduction. The geometrical parameters of the quarter wavelength resonators determine the frequency component at which the noise will be reduced. Besides that, due to the air flow coming out of the compressor, there is phase shift in the wave propagation inside the downstream pipe. Thus the ‘working frequencies’ of the quarter wavelength resonators are moved away. In order to offset this error in the numerical design of resonators, the flow effect analyses are performed by using hybrid CAA modeling method. After this, the relationship between the Mach number of the air flow coming out of the compressors and the shifts in the ‘working frequencies’ is estimated. The relation will be considered in the final design of the resonators, so that the frequency shifts can be offset.

4.1 NUMERICAL OPTIMAL DESIGN

In the numerical design section, the geometric parameters of the quarter wavelength resonator array, which are the depth (l), the diameter (d) of a single resonator, the axial spacing (ΔL), the circumferential spacing (θ) and the number of layers (N), are optimized by using commercial software package COMSOL. The parameter sweep function is used in order to obtain the optimal values. In the first step, the optimal values of the depth and diameter of a single resonator are obtained. Then the geometry shapes of the resonators are fixed and the other parameters are optimized one by one.

Afther numerical simulation, the sensitivy analysis reveals that the performance of the resonator array is significantly sensitive to its depth and diameter. When the depth and diameter are changed by ±5%, the TL value at the target frequency is decreased by 22 to 27 dB.

After optimal design, some other distributions of resonators (staggered distribution, slanted resonator distribution, resonators on expansion pipe and curved pipe models) are also taken into investigation of their noise reduction performance. The staggered distribution of resonator array does not influence the noise reduction performance. The curved pipe configuration with the curvature of 2 meter reduce the TL amplitudes by 17 dB. The 45 degree slanted resonators reduce the bandwidth of the maximum TL performance peak by 30 Hz while the maximum TL value remains the same. The expansion duct with the resonators increases the bandwidth of the maximum TL performance peak by 280 Hz, but reduce the maximum TL value by 6 dB.

4.2 FLOW EFFECT ANALYSES

The flow effect analyses are performed by hybrid CAA simulations. The simulations are separated into fluid dynamics domain and acoustics domain. In fluid dynamics simulation, it is realized by using commercial CFD code ANSYS FLUENT. A steady state simulation is calculated first, and then it is set as initialization of the transient simulation. After fluid dynamics simulations, the results are exported and projected onto the acoustic mesh for aeroacoustic computations. Two aspects of problems are studied in this procedure. One is the phase shift in wave propagation in moving fluid. By simulations with respect to air flow of various speed, the relation between phase shift and flow Mach number can be estimated. On the other hand, the aerodynamic noise generated from the turbulent flow can be extracted. It can be also used in the design of the quarter wavelength resonators for noise estimations.

For the validation of mean flow effect simulation, an in-lab experimental test rig is built. The sound pressures are measured at both the upstream and downstream area. Then the acoustic field are reconstructed by performing cylindrical nearfield acoustic holography, and the transmission loss are calculated. For validations, the transmission loss of the experimental results and the simulated ones are compared.

The flow effect analysis results in the two relations between the frequency shift and the flow speed, and between the TL reduction and the flow speed. From the curve fitting results, the relation between the frequency shift and the flow speed can be represented by $\Delta f = 1918M^2 - 24.21M$. The relation between the TL reduction and the flow speed can be represented by $\mathrm{TL} = 4258.6M^2 - 734.8M + 53.7$.

The aeroacoustic noise is predicted by using hybrid CAA method with the maximum level of less than 60 dB. This maximum level can be ignored, when compared with the overall noise level, 99.3 dB of the Samsung Techwin's compressor. In general, the in-lab experiment shows a good agreement between the experiment and numerical results. The experimental and numerical maximum TL levels match well with each other, although the experimental TL peak shows broader bandwidth than the numerical one. Due to the small TL fluctuation in the experimental data, it is difficult to identify the frequency shift due to the airflow inside the duct.

4.3 FUTURE DIRECTIONS

Although the results presented in this thesis shows good agreement between experimental and simulated ones, in real engineering practice, the noise reduction effect will be easily affected by other factors, for example, the manufacture errors, the instability of the surrounding temperatures, and etc. Regarding to further improvement of the design of the quarter wavelength resonators, it is recommended to make more effort on expanding the bandwidth of the 'working frequencies', so that even when there is phase shift in wave propagation, the noise reduction effect of the quarter wavelength resonator array can still be guaranteed. Regarding to aeroacoustic noise prediction, a simulation with more time steps will be conducted in the future, in order to guarantee the accuracy of simulations.

REFERENCES

[1] J. H. Han, Y. Niu and Y.J. Kim, “Experimental identification of noise radiation characteristics of Samsung Techwin’s Compressor SM5000U,” Research Final Report to Samsung Techwin, 2013.

[2] J. H. Han, N. Ye and Y. J. Kim, “Noise Reduction of Samsung Techwin’s Compressors: Phase II –Design, Implementation, and Evaluation of Noise Control Methods,” Research Final Report to Samsung Techwin, 2014.

[3] Z. Liu and D. L. Hill, “Centrifugal Compressor Noise Reduction by using Helmholtz Resonator Arrays,” Proceedings of the Turbomachinery Symposium.

[4] COMSOL, “Introduction to the Acoustics Module,” User Guide of COMSOL Multiphysics 4.3a, 2012.

[5] X. Shi, C. M. Mak and J. Yang, “Attenuation Performance of a Semi-Active Helmholtz Resonator in a Grazing Flow Duct,” Open Journal of Acoustics, 3, 25-29, 2013.

[6] A. Hersch and B. Walker, “Effect of Grazing Flow on the Acoustic Impedance of Helmholtz Resonators Consisting of Single and Clustered Orifices,” NASA Contractor Report 3177, 1979.

[7] M. J. Lighthill, “On Sound Generated Aerodynamically: I. General Theory,” Proceeding of the Royal Society London, Series A, 211, 564 – 587, 1952.

[8] M. Piellard and C. Bailly, “Validation of a hybrid CAA method. Application to the case of a ducted diaphragm at low Mach number,” AIAA Paper 2008-2873, 2008.

[9] Free Field Technologies, “Actran 2006 Aeroacoustic Solutions,” User’s Manual, 2006.

[10] C. Q. Howard and R. A. Craig, “Adaptive-Passive Quarter-Wave Tube Resonator Silencer,” Proceedings of Acoustics, 2011.

[11] T. Boelkes and I. Hoffmann, “Pipe Diameter and End Correction of a Resonant Standing Wave,” Journal of Physics, Vol.5 – 2, 2011.

[12] J. C. Hardin and S. L. Lamkin, "Computational aeroacoustics - Present status and future promise," IN: Aero- and hydro-acoustics; Proceedings of the Symposium, Ecully, France, July 3–6, 1985 (A87-13585 03-71). Berlin and New York, Springer-Verlag, 1986, p. 253-259

[13] J. H. Seo, Y. J. Moon and B. R. Shin, “Prediction of cavitating flow noise by direct numerical simulation,” Journal of Computational Physics 277, 6511-6531, 2008.

[14] P. Moriarty and P. Migliore, “Semi-Empirical Aeroacoustic Noise Prediction Code for Wind Turbines,” Technical Report, NREL/TP-500-34478, National Renewable Energy Laboratory: Golden, CO.

[15] Fluent Inc., Fluent 6.3 User’s Guide, Sept. 2007.

[16] M. J. Lighthill, “On Sound Generated Aerodynamically. II. Turbulence as a Source of Sound,” Proceeding of the Royal Society London, Series A, 222, 1-32, 1952.

[17] COMSOL, “Introduction to LiveLink for Matlab,” User Guide of COMSOL Multiphysics 4.3a, 2012.

[18] L. E. Kinsler and etc. “Fundamentals of Acoustics,” John Wiley & Sons, Inc., 2000.

[19] A. D. Pierce, “Wave equation for sound in fluids with unsteady inhomogeneous flow,” Journal of Acoustical Society of America, 87:2292–2299, 1990.

[20] W. Möhring, “Modelling low Mach number noise,” Mechanics of Sound Generation in Flows. Springer Verlag, 1979.

[21] C. A. J. Fletcher, “Computational Techniques for Fluid Dynamics. Volume I. Fundamental and General Techniques,” Springer-Verlag, 1988.

[22] D. C. Wilcox, "Turbulence Modeling for CFD". Second edition. Anaheim: DCW Industries, 1998. pp. 174.

[23] Y. Niu and Y. J. Kim, “Nonlinear, dissipative, three-dimensional, planar Nearfield Acoustical Holography based on Westervelt Wave Equation,” Journal of Sound and Vibration, Vol. 332, pp. 952-967, 2013.